Advanced Composites and Hybrid Materials https://doi.org/10.1007/s42114-026-01997-z

Article in Press

Data-driven machine learning models for guiding the preparation of Mn-modified biochar and predicting Cd adsorption

Received: 30 January 2026

Accepted: 20 July 2026

Published online: 28 July 2026

Cite this article as: Wang W., Zhou Z., Wang J. *et al.* Data-driven machine learning models for guiding the preparation of Mn-modified biochar and predicting Cd adsorption. *Adv Compos Hybrid Mater* (2026). https://doi.org/10.1007/s42114-026-01997-z

Weihan Wang, Ziqing Zhou, Jiarui Wang, Haoyu Cao, Bing Geng, Liangguo Luo, Jie Zhu, Changxiong Zhu, Xiangqun Zheng & Liyuan Liu

Data-driven machine learning models for guiding the preparation of Mn-modified biochar and predicting Cd adsorption

Weihan Wang[a,1], Ziqing Zhou[a,1], Jiarui Wang[a], Haoyu Cao[b], Bing Geng[a], Liangguo Luo[a], Jie Zhu[a], Changxiong Zhu[c], Xiangqun Zheng[a,*], Liyuan Liu[a,*]

[a]*Institute of Environment and Sustainable Development in Agriculture, Chinese Academy of Agricultural Sciences, Zhongguancun South Street, Beijing, 100081, China*

[b]*Agro-Environmental Protection Institute, Ministry of Agriculture and Rural Affairs, Tianjin 300191, China*

[c]*College of Environmental Science and Engineering, Hebei University of Science and Technology, Shijiazhuang, 050018, China*

[1] *contributed equally to this manuscript.*

**Corresponding author:*

Liyuan Liu, E-mail: liuliyuan@caas.cn□

Xiangqun Zheng, E-mail: zhengxiangqun@126.com;

Telephone: +86 (022)-82109567.

Abstract

Cadmium (Cd), a typical highly toxic heavy metal, poses serious risks to environmental safety and public health once it enters water bodies. Manganese-modified biochar (Mn-BC) can effectively remove Cd from wastewater. However, the need for complex batch experiments represents a major constraint on its development. The emergence of artificial intelligence provides a new approach to address this

problem. In this study, six machine learning (ML) models were developed to predict the Cd adsorption performance of Mn-BC, aiming to reduce the reliance on complex experimental procedures. Among the six models, the extra trees regressor (ETR) model achieved high prediction accuracy (test $R^2 = 0.970$; root mean square error (RMSE) = 12.982). The ETR model provided insights into the preparation of Mn-BC: the results of feature importance analysis revealed that the initial Cd concentration, biochar dosage, and manganese content were the main contributors to the model output. Additionally, the one-way partial dependence plots revealed that the optimal heating time in the biochar preparation process was 2 h, and the optimal manganese loading reached approximately 10%. To evaluate the practical applicability of the model, Mn-BC was prepared for conducting reverse validation of the ETR model, and the error between the predicted and experimental values was less than 17%. The results of characterization analyses, including X-ray photoelectron spectroscopy (XPS) and X-ray diffraction (XRD), revealed that Mn-BC adsorbed Cd mainly via coordination exchange and surface precipitation. This research not only presents an effective model for predicting adsorbent performance but also provides data-supported insights into the associations between complex preparation and adsorption conditions, thereby offering effective guidance and new insights for practical adsorbent fabrication.

Graphical abstract

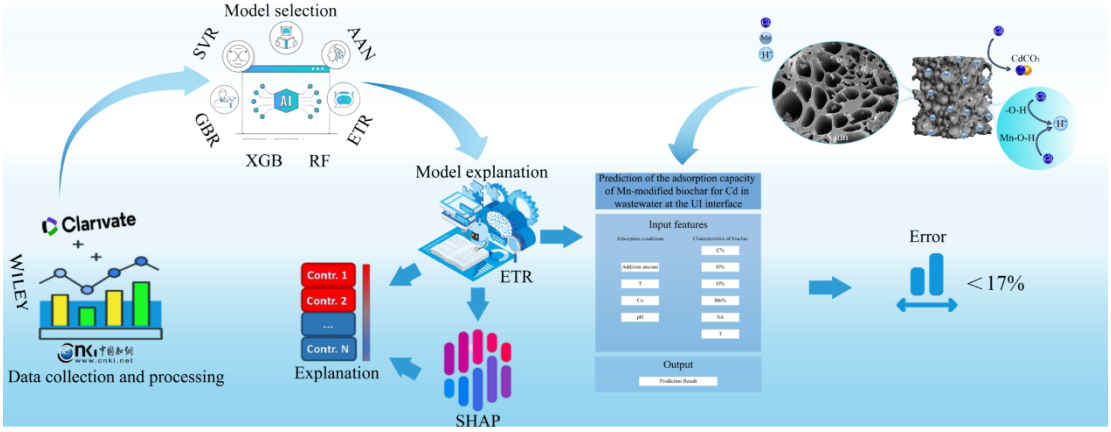

Keywords: Extra Trees Regressor, Manganese-modified Biochar, Adsorbent, Preparation Conditions, Cd

1. Introduction

Cadmium (Cd), a typical highly toxic heavy metal pollutant, is characterized by high toxicity even at low concentrations, nonbiodegradability, and easy migration and accumulation (Sun et al., 2023). Industrial production activities such as electroplating, battery manufacturing, and mining may produce wastewater that contains Cd (Jiang et al., 2024; Li et al., 2025). If not properly controlled, this wastewater can be absorbed by humans and ecosystems through drinking water, the food chain, and bioaccumulation, causing health problems such as kidney damage and bone metabolism disorders and posing serious threats to environmental and human health (Chen et al., 2022). Chemical precipitation readily causes secondary pollution (Xu et al., 2022), while membrane separation and electrochemical methods are costly and thus difficult to apply widely (J. Wang et al., 2023). Adsorption has received significant attention because it is simple to implement, broadly applicable, and easy to couple with existing treatment units (Tian et al., 2023).

Biochar is associated with abundant feedstock sources, a low preparation cost, and abundant surface functional groups, which render it an ideal carrier for adsorbents (Y. Wang et al., 2025). The oxygen-containing functional groups on the surface of biochar (such as carboxyl, hydroxyl, and phenolic hydroxyl groups) provide sites for complexation and ion exchange. However, pristine biochar exhibits limited active-site density, selectivity, and resistance to interference, especially under conditions of multi-ion coexistence or high ionic strength; thus, pristine biochar often fails to satisfy the demand for Cd removal (Mensah et al., 2025).

Loading metal oxides and hydroxides can significantly enhance the adsorption performance of biochar. For example, Fe–Mn bimetal-modified biochar can adsorb Cd(II) and As(III)/As(V) through synergistic mechanisms, including electrostatic attraction and ternary surface complexation (Yin et al., 2023). A mixture of industrial steel slag waste and ginkgo leaves was employed to prepare a novel magnetic adsorbent, which enhanced adsorbent recoverability while enabling the simultaneous adsorption of Cd(II) and As(V) (M. Wang et al., 2023). Mn-Fe bimetal sulfide-modified magnetic biochar derived from hardwood sawdust was synthesized via a stepwise activation–magnetization–sulfidation process, and its use improved the remediation of wastewater contaminated with Cd and Pb (H. Zhang et al., 2025). Among the various metal-modified biochar types, Mn-modified biochar (Mn-BC) exhibits an increased in situ Mn content on its surface, which increases the density of surface active sites and thus enhances its adsorption capacity (Wu et al., 2022).

Manganese oxide exhibits notable surface complexation. Cadmium can be effectively immobilized through coordination exchange and surface precipitation (for example, in 25 mL of a 100 mg/L Cd solution with a pH of 5.0, $Cd(OH)_2$ or $CdCO_3$ can be formed) (Yin et al., 2020) and synergistic interactions with oxygen-containing groups (Fan et al., 2020). Mn also alters the surface charge and acid–base properties of the material, which increases the adsorption stability over a wide range of pH values and enhances the resistance to interference from coexisting ions (Xiao et al., 2020).

Currently, the preparation of adsorbents relies mainly on a large number of experiments, especially batch tests, to determine the optimal preparation and adsorption

conditions. Although advanced tools such as density functional theory (DFT), molecular simulation, and the response surface methodology have been introduced, the preparation of adsorbents still depends on the experience of researchers and their understanding of material properties. Without experimental verification, the adsorption performance cannot be quantified accurately to identify the optimal preparation and adsorption conditions (W. Zhang et al., 2023). However, this method is time consuming and labour intensive, and the adsorbent may not provide the expected results (Shuyan Zhao et al., 2025). With the advent of artificial intelligence, emerging technologies such as machine learning (ML) can greatly reduce the complexity and workload of experimental procedures (Wang and Yao, 2025). ML facilitates the integration of multisource features (material structural parameters, chemical composition, process conditions, and water quality conditions) and facilitates the creation of input–performance maps in nonlinear and strongly coupled systems (Z. Wang et al., 2025). ML enables rapid prediction of the adsorption capacity and significantly reduces the cost of experimental iteration (Chen et al., 2025). After an ML model is established, the key features that determine Cd removal can be identified through feature importance analysis and SHapley Additive exPlanations (SHAP) analysis (Zhao et al., 2024a). ML can integrate the effects of multiple variables, thereby providing a more precise range, which can fulfil a certain guiding role in the design of adsorption materials (Li et al., 2026). Researchers have applied ML to reveal the effect of multivalent background ions (including Ca, K, Na, and Mg) on the adsorption capacity of natural mineral materials for azo dye molecules (Zhao et al., 2024b). By integrating advanced ML techniques

with interpretability tools, researchers have advanced the understanding of ammonia adsorption on biochar (Liu et al., 2025). To rapidly identify effective doping strategies for aluminium-based lithium adsorbents, ML has been employed to guide material screening (R. Zhang et al., 2025). ML models have been adopted to predict the adsorption capacity of arsenite (As(III)) and arsenate (As(V)) on different materials (R^2=0.987; RMSE=3.54) (Huang et al., 2025).

This study focuses on the preparation process of Mn-BC and introduces the preparation conditions, elemental content, pore structure, and other key influencing indicators of Mn-BC. An ML model is established to predict the actual adsorption performance of biochar before its preparation and to provide data-supported guidance for adsorbent preparation to address Cd^{2+} pollution in the target water body, thereby providing directions for reverse design of adsorbents. The design concept of Cd biochar adsorbents is shifted from material preparation–performance testing to customized design of adsorption materials for the target water body.

In this study, ten key features related to the preparation conditions, material properties, and adsorption environment of Mn-BC were selected to predict its Cd adsorption capacity. This study aimed to (1) identify the optimal prediction model through comparative evaluation analysis; (2) quantify the effects of input variables on adsorption performance via feature importance analysis and identify key predictive factors; (3) partially analyse the preparation conditions for biochar; and (4) guide practical experiments with the optimal prediction model, evaluate the prediction performance, and examine possible adsorption mechanisms. Via the use of a data-

driven ML model, this study provides new insights for the rational design and optimization of efficient biochar adsorbents and helps overcome the limitations of traditional methods.

2. Materials and methods

2.1 Data collection

As shown in Fig. 1, the dataset in this study was collected from the Web of Science, Wiley Online Library, and China National Knowledge Infrastructure (CNKI) databases. The publication period was limited to the 2014–2025 range. To enhance the completeness and reproducibility of the literature search, the following search string was adopted: TS = ("Mn" OR "manganese" OR "manganese oxide" OR "manganese-modified" OR "manganese-loaded") AND ("biochar" OR "modified biochar") AND ("cadmium" OR "Cd") AND ("adsorption" OR "removal"). The initial search records were screened according to predefined inclusion and exclusion criteria. Studies were included when they satisfied the following criteria: (i) Mn-BC was employed as the adsorbent; (ii) Cd(II) adsorption was investigated in aqueous solutions; (iii) the adsorption capacity or sufficient data for calculating the adsorption capacity were reported; and (iv) data for the selected feature variables were available without missing values. Studies involving non-Mn-BC, mixed contaminants without separable Cd adsorption data, soil-only immobilization experiments, review articles, duplicated publications, or records with missing key variables were excluded .

Duplicate records were first removed on the basis of the title, DOI, and author information. The title and abstract of the remaining articles were then reviewed,

followed by full-text evaluation. When the same data appeared in both figures and tables, tabulated values were preferentially chosen. With respect to data reported only in figures, WebPlotDigitizer was applied for extraction. After duplicate records and incomplete entries were removed, 27 papers were ultimately retained, yielding 1,016 valid data records (The DOI of the literature and the journal were listed in Table S3).

The input variables were selected to cover the major stages from biochar preparation to Cd adsorption. Specifically, the pyrolysis time (t) represents the preparation conditions; the adsorption temperature (T), biochar dosage, solution pH, and initial Cd concentration (C0) represent the adsorption conditions; and the carbon content (C%), oxygen content (O%), hydrogen content (H%), Mn loading percentage (Mn%), and specific surface area (SA) represent the physicochemical properties of Mn-BC. These ten variables were selected because they are frequently reported in the literature and are directly related to the biochar structure, Mn modification, surface chemistry, and Cd adsorption behaviour.

2.2 Model training

All the algorithms and functions chosen in this study were implemented in Python 3.12.7. The main software packages include pandas 3.0.3, numpy 1.26.4, matplotlib 3.10.9, seaborn 0.13.2, scikit-learn 1.7.2, bayesian-optimization 3.0.1, SHAP 0.49.1, and XGBoost 3.0.5. Six ML algorithms were selected for model development, namely, random forest (RF), extra tree regressor (ETR), gradient boosting regressor (GBR), extreme gradient boosting (XGB), artificial neural network (ANN), and support vector regression (SVR) models (Fig. 1). The coefficient of determination (R^2) was applied to

evaluate the goodness of fit of the models (Shilin Zhao et al., 2025). The differences between the observed and predicted values were quantified on the basis of the RMSE, mean absolute error (MAE), and mean bias error (MBE) (Jie Li et al., 2024).

$$R^2 = 1-\frac{\sum_{i=1}^{n}(y_i-\hat{y}_i)^2}{\sum_{i=1}^{n}(y_i-\bar{y})^2} \quad (1)$$

$$RMSE = \sqrt{\frac{1}{n}\sum_{i=1}^{n}(\hat{y}_i-y_i)^2} \quad (2)$$

$$MAE = \frac{1}{n}\sum_{i=1}^{n}|\hat{y}_i-y_i| \quad (3)$$

$$MBE = \frac{1}{n}\sum_{i=1}^{n}(\hat{y}_i-y_i) \quad (4)$$

where y_i denotes the actual observed value, $\hat{y}_i$ denotes the predicted value, $\bar{y}$ denotes the mean of the observed values, and n denotes the sample size.

2.3 Model interpretation

Through the use of the prebuilt frameworks and libraries provided by scikit-learn, ML modelling (evaluation, interpretation, and application) was conducted. In the dataset, 80% of the data were randomly assigned to the training set, and the remaining 20% were employed to validate the final model. During Bayesian hyperparameter optimization, fivefold cross-validation was applied to the training set containing 80% of the data; four folds were used for training, and one fold was adopted for validation (Zhang et al., 2024). SHAP analysis was employed to interpret feature importance and to help determine the contribution of each feature to the model predictions (Yang et al., 2021). One-way partial dependence analysis was conducted to examine how each input feature affected the output variable, and two-way partial dependence analysis was used to analyse the interaction effects between different features (Yuan et al., 2021).

2.4 Experimental verification under the guidance of machine learning models

Biochar was prepared from corn straw through pyrolysis. Briefly, the raw biomass was washed with deionized water, dried at 50 °C, ground, and sieved through a 20-mesh screen. The dried biomass was then pyrolyzed at 250 °C for 2 h in an oxygen-free atmosphere at a heating rate of 10 °C min^{-1}. The obtained biochar was denoted as BC.

Mn-BC was prepared via the use of a coprecipitation method. Briefly, 1 g of BC was added to 100 mL of a 0.1 mol/L $KMnO_4$ solution, corresponding to a solid-to-liquid ratio of 10 g/L. The suspension pH was adjusted to 10 using a 0.1 mol/L NaOH solution. After ageing at room temperature for 3 h, the suspension was centrifuged, and the precipitate was washed several times with deionized water until the supernatant became neutral. Finally, the obtained Mn-BC was dried at 35 °C overnight.

The morphology and elemental distribution of the samples were characterized via scanning electron microscopy coupled with energy-dispersive spectroscopy (SEM–EDS; TESCAN MIRA LMS). The SA and pore structure were determined through the Brunauer–Emmett–Teller (BET) method (Micromeritics ASAP 2460). The crystalline phases were analysed by X-ray diffraction (XRD; Rigaku SmartLab SE). The surface elemental composition and chemical states were analysed via X-ray photoelectron spectroscopy (XPS; Thermo Scientific ESCALAB 250Xi). The surface functional groups were identified through the use of Fourier transform infrared spectroscopy (FTIR; Thermo Scientific Nicolet iS20). The elemental composition was determined with an elemental analyser (EA; Elementar Unicube), and the Cd concentration was measured via inductively coupled plasma–mass spectrometry (ICP–MS; Agilent 7800 ICP–MS).

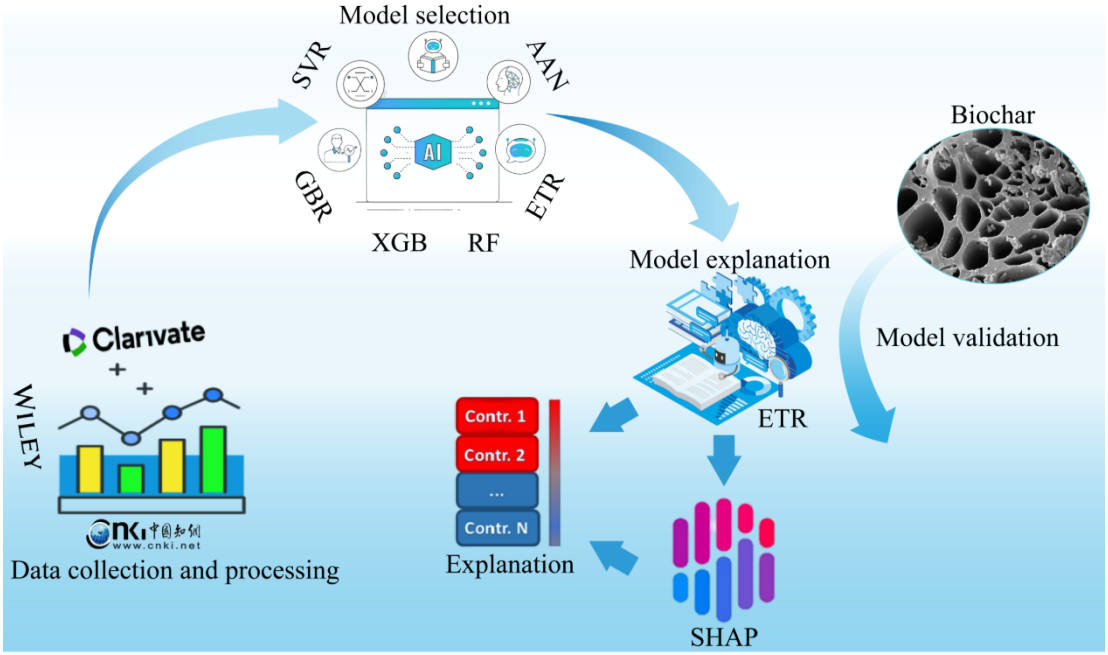

Fig 1. The process of model establishment, evaluation, interpretation and application.

3. Results and discussion

3.1 Statistical analysis of datasets

The different physicochemical properties of biochar and the adsorption conditions are shown in Fig. 2. The elemental composition of biochar, including the contents C, of H, O, and Mn, is shown in Fig. 2a. The C content was generally high, confirming that carbon constituted the main structural framework of biochar. In contrast, the H content remained relatively low, which should not be interpreted only from its absolute mass fraction. For biochar, the atomic H/C ratio is a meaningful indicator of aromaticity, degree of carbonization, and structural stability. A lower H/C ratio usually reflects greater dehydration and dehydrogenation during pyrolysis, accompanied by the formation of more condensed aromatic carbon structures. Conversely, a higher H/C ratio indicates a lower degree of carbonization and greater retention of aliphatic or hydrogen-containing structures. Therefore, the variation in the H content may indirectly

reflect changes in the H/C ratio and the evolution of biochar aromaticity and surface chemistry (Xiao et al., 2016). This structural evolution is closely related to Cd adsorption because excessive carbonization may reduce the number of surface functional groups, whereas moderate carbonization can preserve oxygen- and hydrogen-containing functional groups that contribute to Cd complexation and coordination (J. Zhang et al., 2020). A higher O content in biochar helps increase the abundance of oxygen-containing functional groups on its surface (such as carboxyl and hydroxyl groups), thereby enhancing complexation and ion exchange with Cd^{2+}; therefore, the O content in most biochars is approximately 20% (Sun et al., 2022). As a dopant element, the content of Mn was relatively low, mostly less than 20%. However, the Mn content is likely among the key factors influencing the adsorption of Cd^{2+} by biochar (Wu et al., 2022).

The environmental factors during Cd^{2+} adsorption by biochar, including the biochar dosage, initial solution pH, and adsorption temperature, are shown in Fig. 2b. The amount of added biochar is usually small (< 10 g/L), which might occur because excessive addition of biochar can lead to waste, as the adsorption capacity of biochar is not solely determined by the amount of added biochar but also depends on factors such as the pH (Qu et al., 2023). Because Cd^{2+} precipitates under alkaline conditions, the adsorption solution is generally acidic (< 7), and in real-world Cd^{2+}-containing wastewater, the solution pH is lower than 8. The adsorption temperature is approximately 25 °C, which aims to simulate the ambient temperature in practical adsorption processes (Kong et al., 2024).

The SA of biochar and the initial Cd^{2+} concentration are shown in Fig. 2c. The SA was correlated with the adsorption capacity of biochar; notably, a relatively large surface area likely provides more active sites and pore channels, thereby promoting the physical adsorption and chemical binding of metal ions (J. Wang et al., 2025). Different Cd^{2+} concentration gradients result in distinct concentration differences, which in turn affects the adsorption capacity of biochar (Kong et al., 2023b).

As shown in Fig. 2d, the use of different pyrolysis times affects the adsorption performance of biochar by altering its functional groups. At shorter pyrolysis times, the produced biochar retains more functional groups. With increasing pyrolysis time, the aromaticity of biochar increases, whereas the number of oxygen-containing functional groups decreases, which reduces the number of adsorption sites on the surface of biochar and thus attenuates its adsorption performance (Jishuo Li et al., 2024). Overall, the elemental composition, SA, and external environmental conditions (such as the pH, temperature, and concentration) jointly influence the adsorption behaviour and mechanism of Cd^{2+} on the surface of Mn-BC.

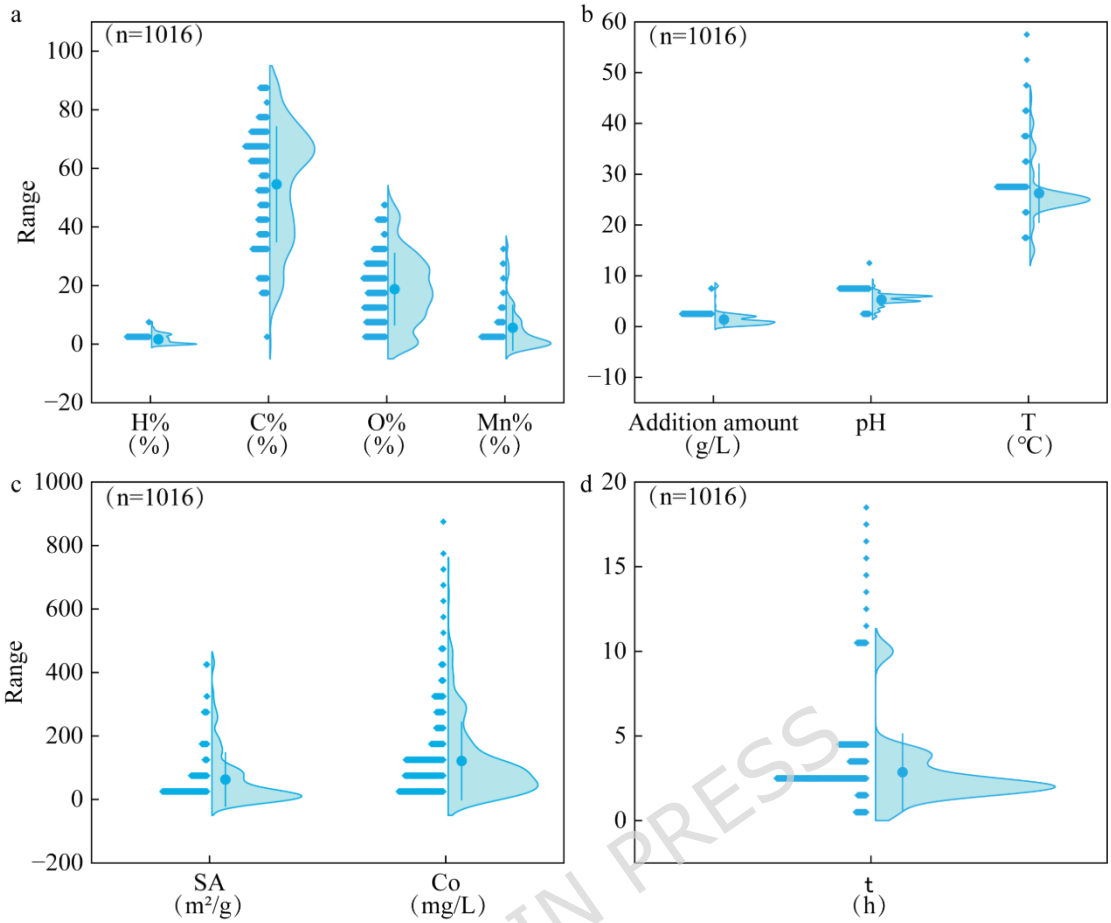

Fig 2. Presents boxplots of each parameter: H%, C%, O%, and Mn%, (a); Addition Amount, pH,T (b); and SA, Co (c); and t (d).

3.2 Pearson correlation coefficient analysis

Pearson's correlation analysis among different variables was conducted to examine the relationships between feature parameters, and the results are shown in Fig. 3. As shown in Fig. 3, significant correlations were observed among most parameters, suggesting potential coupling relationships between the adsorption conditions and the physicochemical properties of biochar.

Ce was significantly correlated with most of the variables, indicating that Cd^{2+} adsorption by Mn-BC was associated with both the adsorption conditions and biochar properties. Specifically, H%, O%, Mn%, and Co were significantly positively correlated with Ce, suggesting that biochars with higher contents of hydrogen- and

oxygen-containing components, higher Mn loadings, and higher initial Cd^{2+} concentrations exhibit higher adsorption capacities. The positive correlation between Co and Ce may be related to the increased concentration gradient at higher initial Cd^{2+} concentrations, which could influence the adsorption performance of biochar (Lian et al., 2020).

C% ($p<0.001$) and H% ($p<0.001$) in the elemental composition of biochar were strongly significantly correlated with t, indicating that variations in the pyrolysis time were associated with changes in H% during biomass pyrolysis and may reflect differences in the abundance of hydrogen-containing functional groups. C% was significantly negatively correlated with H% ($0.01<p<0.001$), O% ($p<0.001$), and Mn% ($p<0.001$), suggesting that biochars with higher C% values contained lower contents of hydrogen- and oxygen-containing components and lower Mn contents. The SA was strongly correlated with most other factors, and these correlations were mainly negative, indicating that a greater SA value was generally associated with lower adsorption performance in this dataset. This result should not be interpreted as a direct adverse effect of the SA itself but may reflect the coupled influence of the preparation conditions. Previous studies have revealed that biochars with higher SA values do not necessarily exhibit higher Cd^{2+} adsorption capacities because Cd^{2+} adsorption by biochar is often governed by chemical interactions such as ion exchange, surface complexation, and precipitation rather than the physical surface area alone (Dai et al., 2021; L. Zhang et al., 2020). This relationship may be related to differences in the preparation process. For example, high pyrolysis temperatures can increase the SA of

biochar while reducing the number of H- and O-containing components and surface functional groups, which may reduce the contribution of chemically active sites to Cd^{2+} adsorption.

Overall, the elemental composition of biochar (C%, O%, Mn%, and SA) and the initial environmental conditions during adsorption jointly affect Cd^{2+} adsorption by Mn-BC.

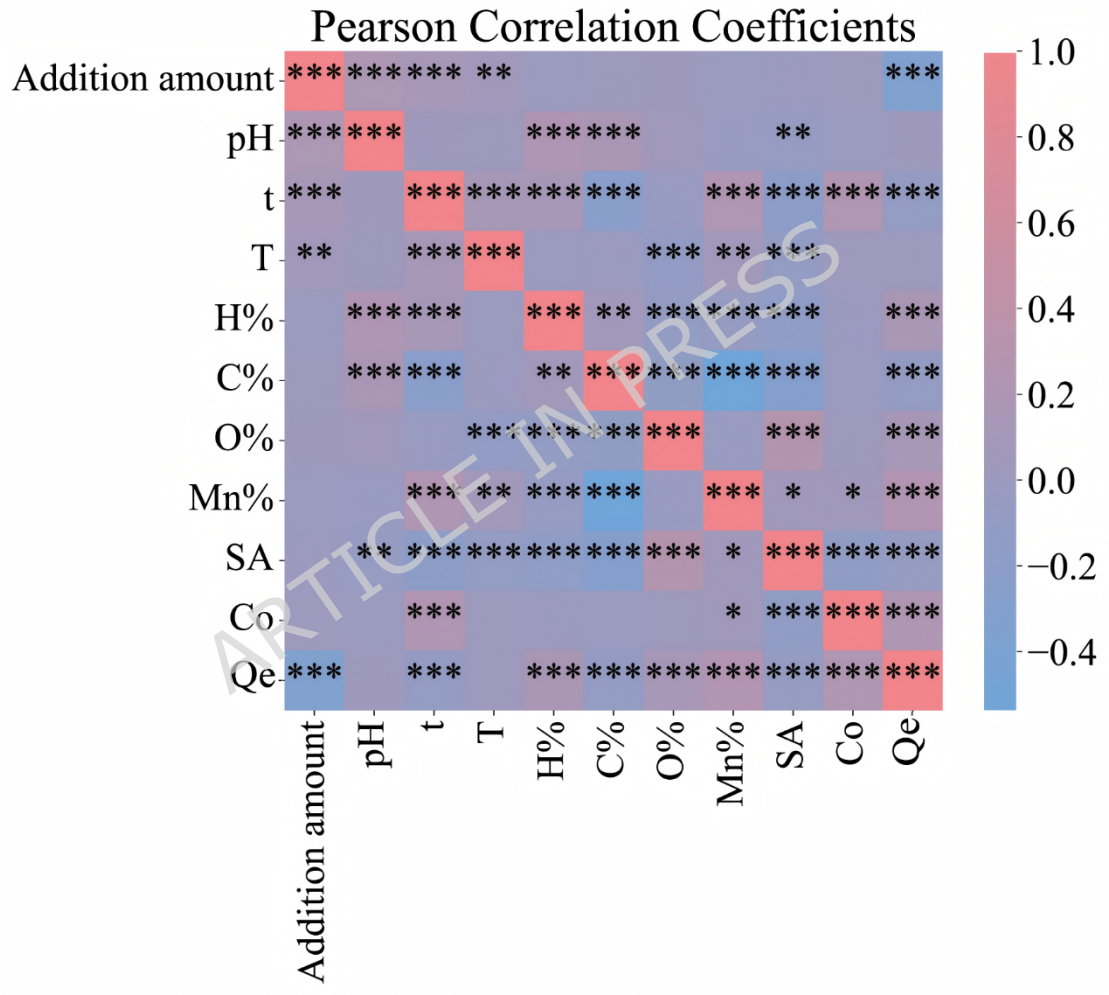

Fig 3. Pearson correlation heatmap with significance levels (the color intensity indicates the strength of correlation between variables, and * significant ** extremely significant *** extraordinarily significant).

3.3 Model prediction

The prediction results of Cd^{2+} adsorption performance obtained with different ML models are shown in Fig. 4. As shown in Fig. 4a–f, the prediction accuracy clearly varied among the models. The ETR model achieved the best performance, with the highest R^2 value (0.970) and the lowest RMSE value (12.982). Compared with the RF and boosting models (GBR and XGB), the ETR model introduces a higher degree of randomness in feature splitting and sample selection, which effectively reduces model variance and avoids overfitting. As a result, this model attained greater stability and generalization for the test set and an improved ability to capture complex nonlinear relationships.

Among the ETR, ANN, and SVR models, the ANN model can simulate highly complex input–output relationships and performs better than linear or tree-based models do (Chellappa et al., 2021). The SVR model was solved globally through the use of kernel techniques, dual transformation, and the sequential minimal optimization (SMO) algorithm, which enables it to gradually approximate complex nonlinear relationships, similar to the GBR model but in a more concise form (Huang et al., 2022). The prediction performance of the ANN and SVR models was worse than that of the ETR model. In terms of R^2, RMSE, MAE, and MBE, the ETR model outperformed the other models.

Significance analysis was conducted for the different models (Fig. S2). Although the difference between the RF and ETR models was not significant, in comparison, the ETR model performed the best among all the algorithms (R^2 = 0.970; RMSE = 12.982; Table 1), suggesting satisfactory prediction performance in resolving high-dimensional

nonlinear relationships and complex feature interactions. Therefore, subsequent analyses were conducted on the basis of the ETR model, including feature importance and interpretability analyses, to identify the key variables contributing to model predictions of the adsorption performance of Mn-BC and to clarify their underlying mechanisms.

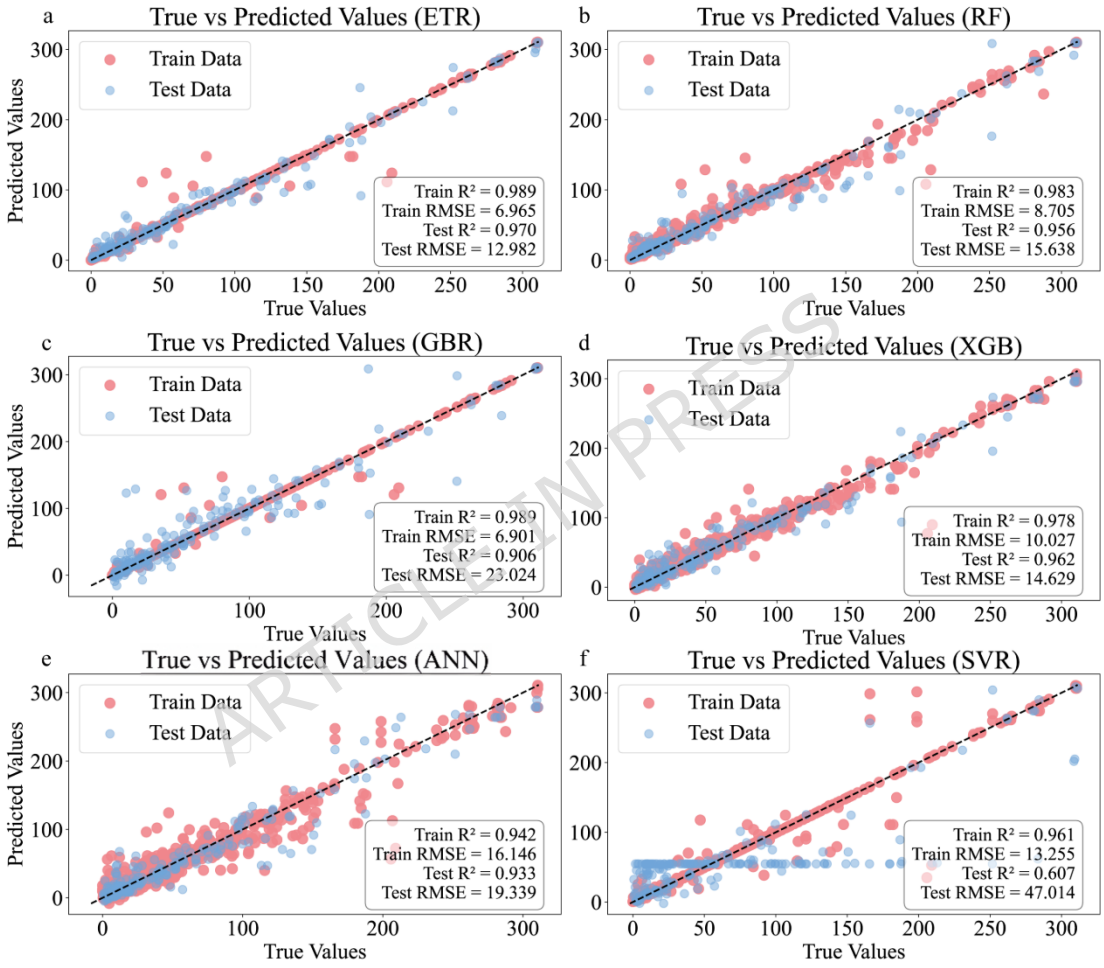

Fig 4. Prediction plots of the ETR (a), RF (b), GBR (c), ANN (e), and SVR (f) models.

Table 1. R^2, RMSE, MAE, and MBE of the ETR, GBR, RF, XGB, ANN, and SVR models.

	R^2		RMSE		MAE		MBE	
	Train	Test	Train	Test	Train	Test	Train	Test
ETR	0.989	0.970	6.965	12.982	0.862	6.498	0.000	0.097
RF	0.983	0.956	8.705	15.638	3.604	8.475	0.227	-1.181

GBR	0.989	0.906	6.901	23.024	0.861	12.200	-0.200	-5.978
XGB	0.978	0.962	10.027	14.629	5.296	9.209	-0.003	-0.585
ANN	0.942	0.933	16.146	19.399	9.183	12.512	-1.823	-2.964
SVR	0.961	0.607	13.255	47.014	2.886	0.607	-0.054	-6.179

3.4 Model fitting and feature importance analysis

The learning curves, residual plots, and feature importance results of the ETR model are shown in Fig. 5, which are used to validate model stability and quantify the contributions of key features. As shown in Fig. 5a–b, with increasing training set size, the prediction accuracy increased notably: the test-set R^2 value first gradually increased and then stabilized, eventually exceeding ~0.9, whereas the RMSE continuously decreased and remained low. This trend suggests that with sufficient samples, the ETR model effectively learned complex feature relationships and achieved suitable generalizability and robustness.

As shown in Fig. 5c, the residuals were randomly distributed around zero, and the residual ranges for the training and test sets were similar. No systematic bias was observed, which indicates that the model yields a good fit (Nandi et al., 2025). These results confirmed the reliability of the ETR model for predicting Cd^{2+} adsorption performance.

The feature importance results obtained with the different methods, including the mean absolute SHAP value (MAS), embedded feature importance (EFI), and permutation feature importance (PFI), are shown in Fig. 5d–f (Neubauer et al., 2024). The three methods yielded highly consistent results, and all the results indicated that Co and Mn% were the main predictors contributing to the prediction of the adsorption capacity. This result was likely due to the relatively high manganese content, which

increased the number of surface active sites and thereby promoted the binding of Cd^{2+}, whereas the notable effect of Co suggested that the initial concentration gradient was among the key forces driving adsorption. This occurred mainly because a relatively large difference in concentration could enhance Cd^{2+} transport, thereby improving the adsorption performance of Mn-BC (Fan et al., 2020). The variables of the addition amount, H%, and O% followed in importance. Although C%, SA, pH, and T also contributed to the observed increase, their importance was relatively low.

Overall, Co and Mn% were the primary factors governing the adsorption performance of Mn-BC.

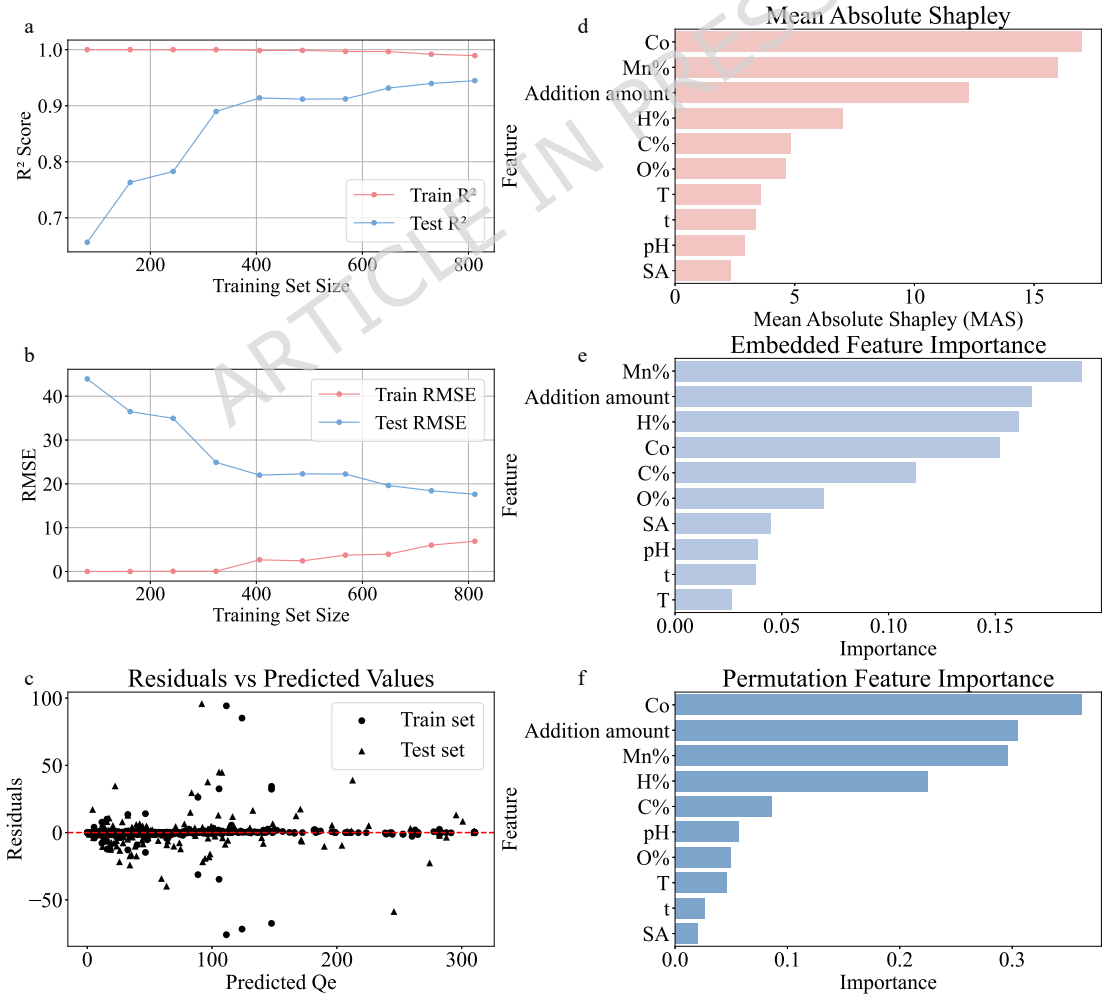

Fig 5. Learning curves of R^2 (a) and RMSE (b); Prediction residual plot (c); PFI (d) and

EFI (e) feature importance analysis; MAS values of feature importance (f).

3.5 Model SHAP analysis and one-way partial dependence analysis

As shown in Figure 6a, there was a significant difference in the distribution of the SHAP values for the input features. The average absolute SHAP values of Co and Mn% were the highest, indicating that they contributed the most to the model predictions. The SHAP values of Co were mainly positive, suggesting that the initial concentration contributed positively to the adsorption capacity. This greater contribution may be related to the adsorption mechanism driven by the concentration gradient in the solution. The positive contribution of the positive SHAP values of Mn% suggested that a higher Mn% value was associated with higher predicted adsorption capacity of the binding sites on the surface of biochar, thereby strengthening its complexation ability. The variables of the addition amount and H% ranked next in importance. The distribution of SHAP values of the addition amount was mainly negative, indicating that an excessive dosage, while reducing Cd^{2+} in water, also decreased the adsorption capacity per unit mass of biochar (Kong et al., 2023a). H% yielded a positive effect, mainly because H% was closely related to surface functional groups; notably, a higher H% value increased the abundance of hydrogen-containing functional groups on the surface of biochar, thereby providing more binding sites for Cd^{2+} (H. Zhang et al., 2025). O%, SA, and t also generated notable effects, indicating that the physicochemical properties of biochar and the adsorption environment played supportive roles in driving Cd^{2+} adsorption by biochar.

The one-way partial dependence plots of the main features are shown in Fig. 6b to explain their effects. With increasing adsorbent dosage, the theoretical adsorption

capacity per unit mass of biochar first decreased rapidly but then stabilized. The partial dependence plots suggested a positive marginal association with the adsorption performance, which might be attributed to the change in hydrogen-containing functional groups (H. Zhang et al., 2020); biochar achieved relatively satisfactory adsorption when the H% value reached approximately 5%. Both O% and Mn% first increased but then decreased, indicating that moderate contents were most favourable for Cd^{2+} adsorption. Excessive Mn loadings may lead to Mn oxide aggregation and a reduced utilization efficiency of active Mn sites, thereby limiting further improvement in the Cd adsorption performance (H. Zhang et al., 2020); the adsorption performance was better when Mn% and O% reached approximately 10% and 35%, respectively. The SA first increased but then decreased, possibly because achieving an excessively high surface area requires a longer carbonization time. For $t > 4$ h, the adsorption performance decreased considerably. Therefore, a lower SA could help facilitate the retention of surface functional groups and thus enhance adsorption. The pyrolysis time should be < 4 h. Although the SA value increased, many binding sites might be lost. The one-way partial dependence plots of the pH, T, and Co indicated that the adsorption capacity increased gradually as the values of these variables increased (Fig. S1).

Co and Mn% were the most influential in model prediction, while the C, H, and O ratios and pore-structure parameters also participated in regulating the adsorption behaviour. The combination of SHAP and partial dependence plot analyses not only supported the reliability and interpretability of the model but also provided a theoretical basis for clarifying the key mechanisms underlying Cd^{2+} adsorption by biochar.

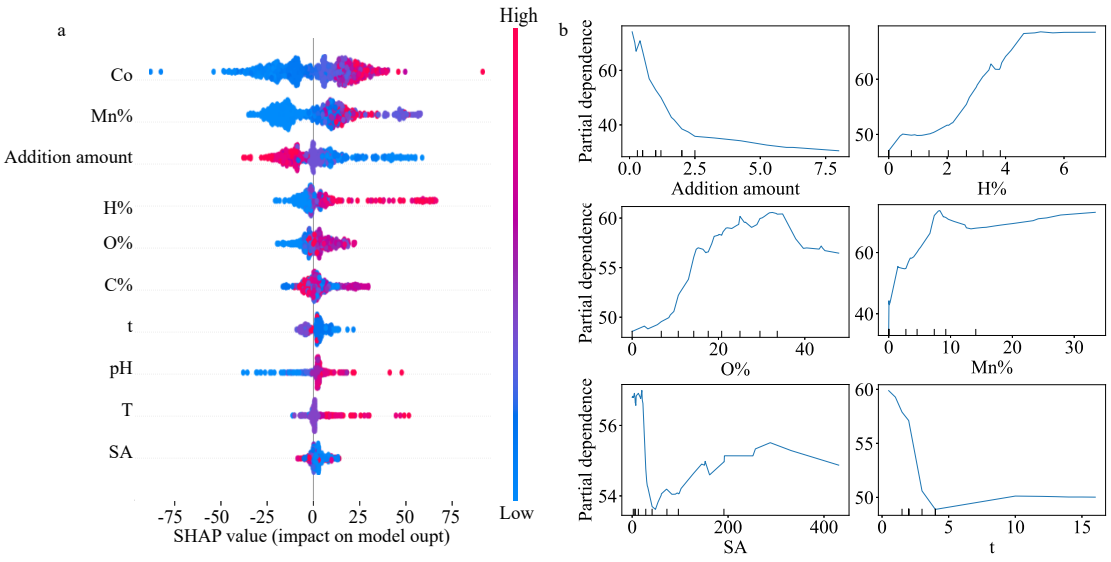

Fig 6. SHAP values of feature importance (a); The one-way partial dependence plot of each input feature in the ETR model (b).

3.6 Two-way partial dependence analysis

To clarify the effect of loading and the role of Mn in biochar, two-way partial dependence plots were created to analyse how different factors interact with Mn%. The bivariate interaction effects between the Mn-doping content (Mn%) and other key features (Co, pH, T, C%, H%, O%, SA, t, and addition amount) on the Cd^{2+} adsorption performance are shown in Fig. 7. The multiple influences of the predicted adsorption capacity under different parameter combinations are shown in Fig. 7a–i.

As shown in Fig. 7a, the interaction between Co and Mn% was significant. When Mn% was low, the adsorption capacity increased notably with increasing Co, whereas in the high-Mn% region, the positive effect of Co gradually weakened. This result indicates that under high-doping conditions, the number of Mn-provided surface reactive sites was close to saturation. Thus, increasing the initial concentration further yielded a limited promotional effect. As Mn% continuously increased, the adsorption

capacity first decreased but then increased, possibly because a higher Mn% value promoted metal aggregation on the surface of biochar and thus reduced the number of available binding sites. The combined effect of the pH and Mn% is shown in Fig. 7b, indicating that the positive effect of Mn doping was greatest under near-neutral conditions (pH: 6–7) and that a Mn content of approximately 10% resulted in relatively satisfactory adsorption performance.

The interactive effects of the temperature (T) and the elemental composition of biochar (C%, H%, and O%) with Mn% are shown in Fig. 7c–f. With increasing temperature, the overall adsorption performance improved, and biochar with higher Mn% values exhibited better Cd^{2+} removal at increased temperatures. This result indicates that the adsorption process is endothermic, which is consistent with the findings of previous studies (Yin et al., 2023). When C% ranged from 50–75%, positive synergy with Mn was observed, indicating that a higher degree of carbonization and metal doping jointly enhanced Cd^{2+} complexation. When Mn% reached approximately 10%, increasing H% improved the adsorption performance of biochar, which is likely related to the presence of hydrogen-containing functional groups on the surface of biochar. The changes in O% indicated that under both low- and high-Mn% conditions, O contents ranging from 15–40% are beneficial for Cd^{2+} adsorption, which might be associated with different Mn valence states (Liu et al., 2023).

As shown in Fig. 7g–i, the SA, t, and addition amount also exhibited significant interaction effects with Mn%. When the SA and Mn% were low, the adsorption capacity increased. Reducing the reaction time also improved the adsorption

performance, which might be attributed to the preservation of surface functional groups. The adsorption performance was better at a dosage of approximately 1 g/L.

Overall, the Cd^{2+} adsorption performance was controlled by Mn doping and multiparameter synergy. Increasing Mn% significantly amplified the positive effects of environmental and structural factors (such as the pH, temperature, and SA). However, an excessively high doping level could cause active-site saturation and aggregation effects, thereby limiting further improvement. A Mn content of approximately 10% promoted Cd^{2+} adsorption by biochar. These results confirm the key role of Mn doping in regulating Cd^{2+} adsorption by biochar.

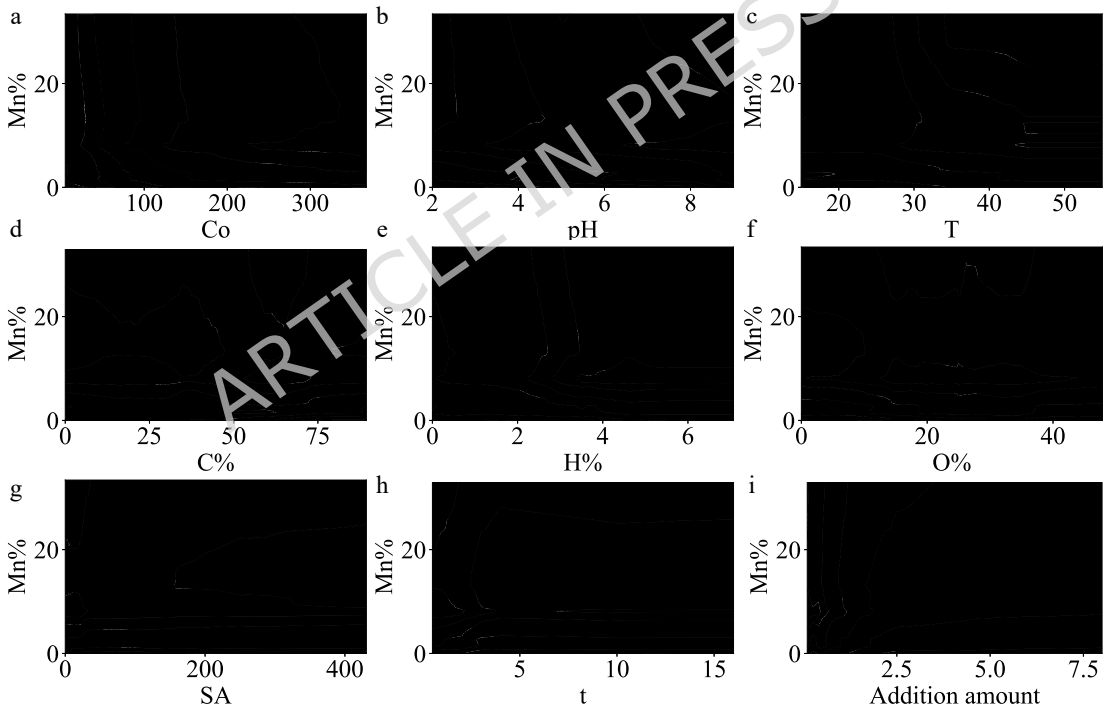

Fig 7. Two-way partial dependence plot of each input feature in the ETR model.

3.7 Experimental verification

To validate the model performance, rice husk biochar was modified with potassium permanganate under the guidance of the ETR model (Table S1). Under

different experimental conditions, the error between the actual performance of Mn-BC and the predicted performance was less than 17% (Table 2). This result indicates that the ETR model accurately predicted the adsorption performance of Mn-BC and provided effective guidance for its preparation.

Table 2. The predicted values output by the model and the actual adsorption capacity.

Predicted value	Actual adsorption capacity	Error
81.366	94.840	16.559
108.243	97.047	-10.343
84.280	95.371	13.160

3.8 SEM–EDS analysis

To validate the model performance, rice husk biochar was modified with potassium permanganate to obtain BC and Mn-BC. The micromorphology and elemental distribution of Mn-BC before and after Cd^{2+} adsorption are shown in Fig. 8. The surface structure of the pristine biochar is shown in Fig. 8a. At 5 μm, the biochar exhibited a three-dimensional porous network with a relatively uniform pore distribution and interconnected pore walls, forming a rich pore channel system. This structure facilitated rapid diffusion and mass transfer of Cd^{2+} in solution and provided sufficient contact interfaces for adsorption (Liu et al., 2022). The structures of Mn-BC and biochar after Cd adsorption are shown in Fig. 8b–c. Compared with the data in Fig. 8a, obvious precipitated substances were observed, indicating that Mn was successfully loaded onto the surface of biochar (the elemental maps in Fig. 8h–i and the EDS spectra also support this finding). These features were clearer at 500 nm. As shown in Fig. 8d–f, more precipitates occurred in the pore channels, which was likely due to successful Mn loading and Cd adsorption via surface precipitation. Moreover, the presence of Mn and

Cd in Fig. 8h–i confirmed the successful capture of Mn and Cd on the surface of biochar. The increased amounts of precipitates suggested an effective Mn content on the surface of biochar and within the pores, and after Cd^{2+} adsorption, select particles likely formed Cd–Mn complexes or precipitates with Cd^{2+}. This finding in turn indicates that Mn-BC adsorbed Cd^{2+} through chemisorption and surface reactions. The EDS spectra confirmed the presence of C, O, Mn, and Cd in the samples, and the characteristic Cd peak after adsorption indicated that Cd^{2+} was adsorbed on the surface of Mn-BC. Overall, the combined SEM and EDS results confirmed that Mn was successfully loaded onto the surface of biochar and enabled efficient capture of Cd^{2+}.

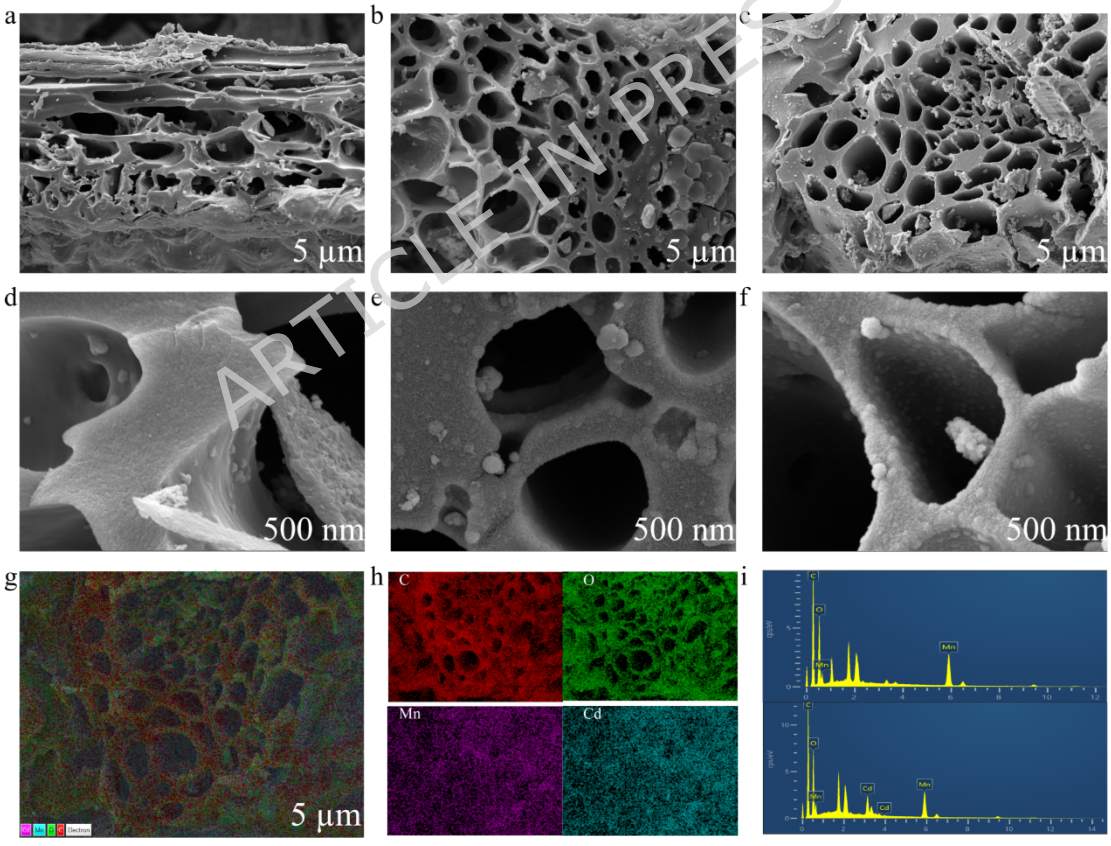

Fig 8. 5 μm scanning electron microscope images of BC (a), Mn-BC (b), and Cd-Mn-BC (c); 500 nm scanning electron microscope images of BC (d), Mn-BC (e), and Cd-Mn-BC (f); EDS mapping:C, O, Mn, Cd elemental distribution of the Cd-Mn-BC (g□

h); EDS spectrum of BC-Mn-BC (i).

3.9 Performance and mechanistic analysis

To investigate the Mn-BC adsorption mechanism, the biochar samples before and after adsorption were characterized. The adsorption capacity and removal efficiency of Mn-BC at different initial concentrations and dosages are shown in Fig. 9a. At a dosage of 1 g/L, Mn-BC achieved a high removal efficiency close to 100%, whereas at 2 g/L, the removal efficiency decreased. This result indicates that at a concentration of 1 g/L, Mn-BC removed Cd^{2+} from water more effectively. When the initial concentration was 100 or 200 mg/L, the adsorption capacity changed only slightly, suggesting that Cd^{2+} adsorption by Mn-BC stabilized. This likely occurred because the adsorption sites on the surface of Mn-BC approached saturation. Therefore, increasing the initial concentration did not significantly increase the adsorption capacity. The N_2 adsorption–desorption isotherm of Mn-BC is shown in Fig. 9b. The curve corresponded to a type-IV isotherm with an H3 hysteresis loop, likely because of the presence of mesopores and slit-shaped pores. The adsorption amount increased continuously with increasing relative pressure, indicating that the mesoporous structure provided sufficient pore space, and the hysteresis loop confirmed the presence of mesopores (Wang et al., 2024). The mesoporous structure provided Mn-BC with abundant pore channels and a high SA, thereby offering favourable conditions for Cd^{2+} adsorption. The XRD patterns of Mn-BC before and after Cd^{2+} adsorption are shown in Fig. 9c. After potassium permanganate modification, clear Mn_3O_4 peaks (PDF#: 24-0734) were identified, indicating that Mn was successfully loaded onto the surface of Mn-BC. Cd occurred in

the material mainly in a precipitated form as $CdCO_3$ (PDF#: 42–1342). The formation of $CdCO_3$ likely resulted from carbonate functional groups remaining after biochar carbonization or from dissolved CO_2 in the solution reacting with Cd^{2+} to form precipitates (Y. Zhang et al., 2023).

Before adsorption, the C 1s spectrum of Mn-BC was deconvoluted into three components, namely, 284.4 eV (C–C/C–H), 285.53 eV (C–C/C–OH), and 288.15 eV (C–O/C=O) (C 1s XPS spectra are shown in Fig. 9d). After adsorption, the relative proportion of C–C/C–H decreased from 62.89% to 49.02%, which was likely caused by Cd^{2+} adsorption.

The O 1s XPS spectra in Fig. 9e reveal that before adsorption, the O 1s peaks of Mn-BC were assigned to 532.53 eV (H_2O), 530.73 eV (M–OH), and 529.62 eV (M–O). After adsorption, the binding energy of the M–O proportion increased from 38.97% to 40.97%. The proportion of M–OH increased from 9.75% to 14.98% (a binding energy shift of ~0.15 eV), whereas the proportion of H_2O decreased from 51.28% to 44.05% (a shift of 0.11 eV). These changes could be attributed mainly to coordinated exchange between surface functional groups and Cd^{2+}, which resulted in the immobilization of Cd^{2+}. After Cd^{2+} adsorption, Mn–O–R (R: functional group) or Cd–O species formed on the surface of Mn-BC (Yin et al., 2020). The Mn $2p_{3/2}$ peak was deconvoluted into Mn(III) (641.61 eV) and Mn(IV) (642.63 eV), together with a satellite peak, indicating that Mn-BC was successfully loaded with Mn(III) and Mn(IV) (Lin et al., 2025). In the Cd XPS spectrum, the characteristic peaks of Cd $3d_{3/2}$ and Cd $3d_{5/2}$ were located at 411.57 and 404.82 eV, respectively, corresponding to CdO and

$CdCO_3$, respectively (Henríquez et al., 2023). As shown in Fig. 9g, the valence state of Cd(II) remained unchanged after adsorption, indicating that Mn-BC removed Cd(II) mainly through adsorption rather than oxidation or reduction processes (Yin et al., 2023). The Mn-BC adsorption mechanism is shown in Fig. 9h.

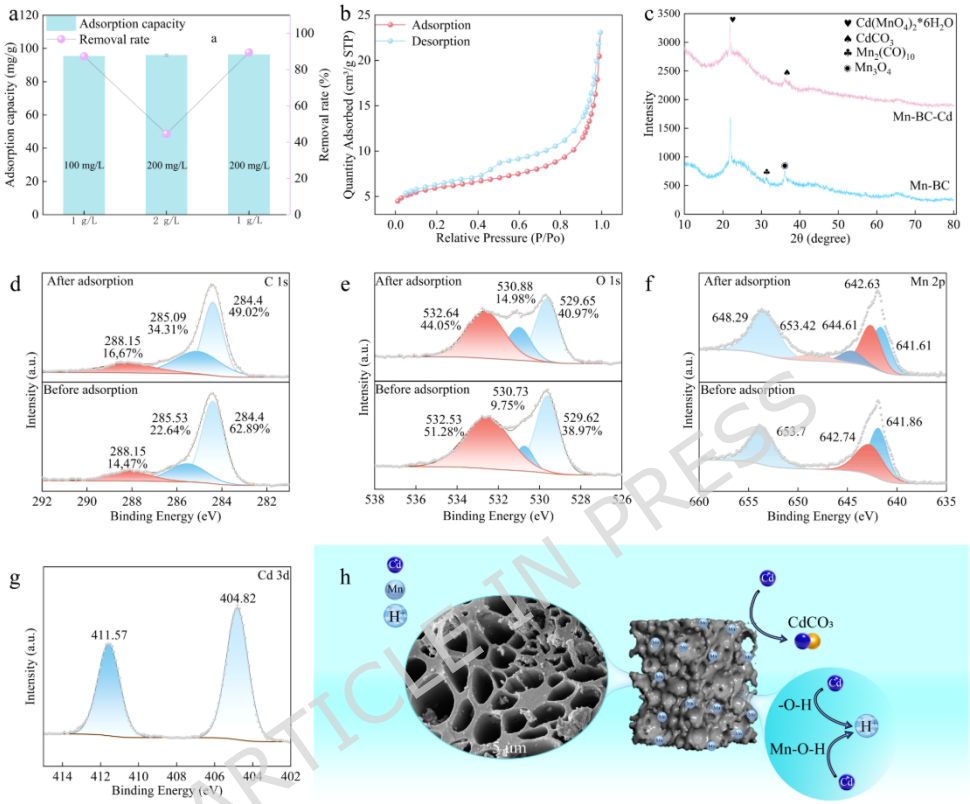

Fig 9. The adsorption capacity and removal rate of Mn-BC (a); The N_2 adsorption-desorption isotherms of Mn-BC (b); XRD (c); High-resolution XPS spectra of C 1s (d), O 1s (e), Mn 2p (f), Cd 3d (g); Adsorption mechanism diagram (h).

3.10 Prospects and limitations

In this study, ML models were employed to preliminarily explore how the preparation conditions and adsorption environment affect the Cd adsorption performance of Mn-BC, but further research remains needed. The main limitations are as follows: first, the dataset size remains relatively small. Thus, the dataset should be

expanded to enhance model stability and generalizability. Second, the current data do not cover additional microscopic material characteristics (such as functional groups and Mn content forms), which prevents a more in-depth investigation of the adsorption mechanism and creates a barrier to mechanism elucidation. This study did not focus on in-depth mechanistic analysis. In future work, advanced theoretical methods such as molecular dynamics and DFT simulations should be combined with ML methods to analyse the adsorption process at the molecular and atomic levels, thereby providing more detailed theoretical support for clarifying the mechanism underlying Cd adsorption on Mn-BC.

4. Conclusions

In this study, an ML framework for predicting the adsorption behaviour of cadmium by Mn-BC was developed. The ETR model achieved the best overall prediction performance and was subsequently employed for further interpretation and experimental verification. The model interpretation results revealed that an effective manganese–biochar design should comprehensively balance the manganese loading, pyrolysis conditions, and the retention of surface functional groups rather than merely increasing the metal content or SA. The experimental verification results in turn confirmed the applicability of the model-guided strategy. The increase in the cadmium adsorption capacity of Mn-BC was attributed mainly to the synergistic effects of surface complexation, coordination exchange, and surface precipitation. In summary, this study demonstrated that interpretable ML can be used to not only predict the adsorption performance but also provide practical guidance for the design of metal-modified

biochar adsorbents.

Supporting Information

The Supporting Information has been supplemented with the one-way partial dependence plots of each input feature in the ETR model, the Mn-BC data obtained under different conditions for model validation, the porosimetry parameters of Mn-BC, and the DOI and journal information of the cited literature. The original data have been uploaded to GitHub and are available at: https://github.com/wwwliuliuliuwww-svg/Mn-biochar-Cd-adsorption-ML.

Declaration of Competing Interest

The authors declare that they have no known competing financial interests or personal relationships that could have appeared to influence the work reported in this paper.

Acknowledgment

This work was supported by National Key Research and Development Program of China (2024YFD1600204), National Natural Science Foundation of China (42407035)□ Central Public-interest Scientific Institution Basal Research Fund.The authors extend their gratitude to Theoretical and Computational Chemistry Team from Shiyanjia Lab (www.shiyanjia.com) for providing invaluable assistance.

References

Chellappa, R., Theodoridis, S., Van Schaik, A., 2021. Advances in machine learning and deep neural networks. Proceedings of the IEEE 109, 607–611.

Chen, H., Zhang, R., Qu, X., Shan, T., Wang, Y., Zhou, R., Zhao, S., 2025. Optimizing Cu2+ adsorption prediction in Undaria pinnatifida using machine learning and isotherm models. Journal of Hazardous Materials 492, 138202.

Chen, L., Guo, L., Liao, P., Xiong, Q., Deng, X., Gao, H., Wei, H., Dai, Q., Pan, X., Zeng, Y., 2022. Effects of biochar on the dynamic immobilization of Cd and Cu and rice accumulation in soils with different acidity levels. Journal of Cleaner Production 372, 133730.

Dai, W., Xu, M., Zhao, Z., Zheng, J., Huang, F., Wang, H., Liu, C., Xiao, R., 2021a. Characteristics and quantification of mechanisms of Cd2+ adsorption by biochars derived from three different plant-based biomass. Arab. J. Chem. https://doi.org/10.1016/j.arabjc.2021.103119

Dai, W., Xu, M., Zhao, Z., Zheng, J., Huang, F., Wang, H., Liu, C., Xiao, R., 2021b. Characteristics and quantification of mechanisms of Cd2+ adsorption by biochars derived from three different plant-based biomass. Arab. J. Chem. https://doi.org/10.1016/j.arabjc.2021.103119

Dai, W., Xu, M., Zhao, Z., Zheng, J., Huang, F., Wang, H., Liu, C., Xiao, R., 2021c. Characteristics and quantification of mechanisms of Cd2+ adsorption by biochars derived from three different plant-based biomass. Arab. J. Chem. https://doi.org/10.1016/j.arabjc.2021.103119

Fan, Z., Zhang, Q., Li, M., Sang, W., Qiu, Y., Wei, X., Hao, H., 2020. Removal behavior and mechanisms of Cd (II) by a novel MnS loaded functional biochar: Influence of oxygenation. Journal of Cleaner Production 256, 120672.

Henríquez, R., Mestra-Acosta, A.S., Grez, P., Muñoz, E., Sessarego, G., Navarrete-Astorga, E., Dalchiele, E.A., 2023. High-performance asymmetric supercapacitor based on a CdCO3/CdO/Co3O4 composite supported on Ni foam – part II: a three-electrode electrochemical study. RSC Adv. https://doi.org/10.1039/d3ra00499f

Huang, H., Wei, X., Zhou, Y., 2022. An overview on twin support vector regression. Neurocomputing 490, 80–92.

Huang, J., Ashraf, W.M., Ansar, T., Abbas, M.M., Tlija, M., Tang, Y., Guo, Y., Zhang, W., 2025. Optimisation led energy-efficient arsenite and arsenate adsorption on various materials with machine learning. Water Research 271, 122815.

Jiang, X., Liu, Z., Yan, B., Zhao, L., Chen, T., Yang, X., 2024. Effects of active silicon amendment on Pb(II)/Cd(II) adsorption: Performance evaluation and mechanism. Journal of Hazardous Materials 478, 135614. https://doi.org/10.1016/j.jhazmat.2024.135614

Kong, H., Li, Q., Zheng, X., Chen, P., Zhang, G., Huang, Z., 2023a. Lanthanum modified chitosan-attapulgite composite for phosphate removal from water: Performance, mechanisms and applicability. International Journal of Biological Macromolecules 224, 984–997.

Kong, H., Wang, J., Zhang, G., Shen, F., Li, Q., Huang, Z., 2023b. Synthesis of three-dimensional porous lanthanum modified attapulgite chitosan hydrogel bead for phosphate removal: Performance, mechanism, cost-benefit analysis. Separation and Purification Technology 320, 124098.

Kong, H., Wang, W., Wang, J., Zhang, G., Shen, F., Jiang, H., Li, Q., Huang, Z., 2024. New insights into Lanthanum-Calcium bimetal for phosphate removal: Performance, molecular dynamics and life cycle assessment. Separation and Purification Technology 351, 128038.

Li, H., Shi, Y., Liu, J., Ba, Z., Liu, S., Yan, B., Liang, D., Xie, Y., 2026. Elucidating microplastic

adsorption mechanisms in biomass composite materials through interpretable machine learning. Journal of Hazardous Materials 501, 140700. https://doi.org/10.1016/j.jhazmat.2025.140700

Li, Jie, Pan, L., Huang, Y., Liu, X., Ye, Z., Wang, Y., 2024. Biochar design for antibiotics adsorption via a hybrid machine-learning-based optimization framework. Separation and Purification Technology 348, 127666.

Li, Jishuo, Xu, K., Yao, X., Liu, J., 2024. Investigation of biomass slow pyrolysis mechanisms based on the generation trends in pyrolysis products. Process Safety and Environmental Protection 183, 327–338.

Li, W., Zhang, L., Su, T., Luo, X., Xie, X., Qin, Z., 2025. Carboxymethyl cellulose sodium/bentonite composite adsorbent for Cd(II) adsorption from wastewater. Adv. Compos. Hybrid Mater. https://doi.org/10.1007/s42114-024-01185-x

Lian, W., Yang, L., Joseph, S., Shi, W., Bian, R., Zheng, J., Li, L., Shan, S., Pan, G., 2020. Utilization of biochar produced from invasive plant species to efficiently adsorb Cd (II) and Pb (II). Bioresource Technology 317, 124011. https://doi.org/10.1016/j.biortech.2020.124011

Lin, H., Li, Xiaoyin, He, J., Li, Xinru, Meng, K., Dong, Y., 2025. Fe/Mn-modified rapeseed straw biochar for selective removal of Pb2+ and Cd2+ from acid mine drainage: adsorption performance and mechanism. Journal of Analytical and Applied Pyrolysis 107393.

Liu, B., Chen, T., Wang, B., Zhou, S., Zhang, Z., Li, Y., Pan, X., Wang, N., 2022. Enhanced removal of Cd2+ from water by AHP-pretreated biochar: Adsorption performance and mechanism. Journal of Hazardous Materials 438, 129467.

Liu, C., Balasubramanian, P., An, J., Li, F., 2025. Machine learning prediction of ammonia nitrogen adsorption on biochar with model evaluation and optimization. Npj Clean Water 8, 13.

Liu, Z., He, M., Tang, L., Shao, B., Liang, Q., Wu, T., Pan, Y., Zhang, X., Luo, S., He, Q., 2023. Dual redox cycles of Mn (II)/Mn (III) and Mn (III)/Mn (IV) on porous Mn/N co-doped biochar surfaces for promoting peroxymonosulfate activation and ciprofloxacin degradation. Journal of Colloid and Interface Science 634, 255–267.

Mensah, A.K., Sekyi-Annan, E., Adams, S., Okyere, H., Issaka, F., Asante, P.C., Yakubu, H.G., Tay, C.K., 2025. Potentially toxic elements in flooded-gold-mine fields: compost stabilises Cd, biochar and manure mobilize As and Pb. Journal of Hazardous Materials 139736.

Nandi, B., Patel, G., Das, S., 2025. Machine learning prediction of flow-induced scour depth around isolated pier comparing stand-alone and ensemble models. Engineering Applications of Artificial Intelligence 156, 111318.

Neubauer, A., Brandt, S., Kriegel, M., 2024. Relationship between feature importance and building characteristics for heating load predictions. Applied Energy 359, 122668.

Qu, J., Che, N., Niu, G., Liu, L., Li, C., Liu, Y., 2023. Iron/manganese binary metal oxide-biochar nano-composites with high adsorption capacities of Cd2+: Preparation and adsorption mechanisms. Journal of Water Process Engineering 51, 103332.

Sun, L., Gong, P., Sun, Y., Qin, Q., Song, K., Ye, J., Zhang, H., Zhou, B., Xue, Y., 2022. Modified chicken manure biochar enhanced the adsorption for Cd2+ in aqueous and immobilization of Cd in contaminated agricultural soil. Science of the Total Environment 851, 158252.

Sun, Y., Liu, C., Gao, Y., Zhang, T., Jia, Y., Wang, S., 2023. All-in-one strategy to prepare molded biochar with magnetism from sewage sludge for high-efficiency removal of Cd (II). Journal of Hazardous Materials 454, 131488.

Tian, H., Peng, S., Zhao, L., Chen, Y., Cui, K., 2023. Simultaneous adsorption of Cd (II) and

degradation of OTC by activated biochar with ferrate: Efficiency and mechanism. Journal of Hazardous Materials 447, 130711.

Wang, J., Wei, X., Kong, H., Zheng, X., Guo, H., 2023. Hydrothermal Ammonia Carbonization of Rice Straw for Hydrochar to Separate Cd(II) and Zn(II) Ions from Aqueous Solution. Polymers. https://doi.org/10.3390/polym15234548

Wang, J., Wei, X., Shen, Y., Kong, H., Wang, W., Smith Jr, R.L., Guo, H., 2025. Mitigation of phosphorus contamination from livestock farms with La-containing hydrochar adsorbent. Separation and Purification Technology 359, 130465.

Wang, M., Wang, X., Zhang, M., Han, W., Yuan, Z., Zhong, X., Yu, L., Ji, H., 2023. Treatment of Cd (II) and As (V) co-contamination in aqueous environment by steel slag-biochar composites and its mechanism. Journal of Hazardous Materials 447, 130784.

Wang, Q., Yao, Y., 2025. Harnessing machine learning for high-entropy alloy catalysis: a focus on adsorption energy prediction. npj Computational Materials 11, 91.

Wang, W., Kong, H., Wang, J., Zhang, G., Shen, F., Liu, F., Huang, Z., 2024. Lanthanum-calcium bimetallic-modified attapulgite-chitosan hydrogel beads for efficient phosphate removal from water: Performance evaluation, mechanistic and life cycle assessment. Carbohydrate Polymers 338, 122183.

Wang, Y., Zeng, W., Wan, X., Wang, L., Lei, M., Chen, T., 2025. Modeling the removal of Cd (II) and Pb (II) from aqueous solutions by biochar derived from arsenic hyperaccumulator Pteris vittata. Journal of Environmental Management 381, 125280.

Wang, Z., Wang, B., Liu, Q., Huo, X., Chang, T., Sun, J., Zhao, Z., Wang, G., Liu, J., 2025. Predicting heavy metals adsorption on microplastics and unraveling the adsorption mechanism with machine learning methods. Surfaces and Interfaces 72, 107101. https://doi.org/10.1016/j.surfin.2025.107101

Wu, P., Cui, P., Zhang, Y., Alves, M.E., Liu, C., Zhou, D., Wang, Y., 2022. Unraveling the molecular mechanisms of Cd sorption onto MnOx-loaded biochar produced from the Mn-hyperaccumulator Phytolacca americana. Journal of Hazardous Materials 423, 127157.

Xiao, J., Hu, R., Chen, G., Xing, B., 2020. Facile synthesis of multifunctional bone biochar composites decorated with Fe/Mn oxide micro-nanoparticles: physicochemical properties, heavy metals sorption behavior and mechanism. Journal of Hazardous Materials 399, 123067.

Xiao, X., Chen, Z., Chen, B., 2016. H/C atomic ratio as a smart linkage between pyrolytic temperatures, aromatic clusters and sorption properties of biochars derived from diverse precursory materials. Sci. Rep. https://doi.org/10.1038/srep22644

Xu, C., Zhao, W., Ma, H., Wang, H., Wang, Y., 2022. Tailored design of well-defined hierarchical nitrogen-doped carbon via salt-confined strategy for selective Cd(II) adsorption. Chemical Engineering Journal 446, 137222. https://doi.org/10.1016/j.cej.2022.137222

Yang, H., Huang, K., Zhang, K., Weng, Q., Zhang, H., Wang, F., 2021. Predicting heavy metal adsorption on soil with machine learning and mapping global distribution of soil adsorption capacities. Environmental Science & Technology 55, 14316–14328.

Yin, G., Chen, X., Sarkar, B., Bolan, N.S., Wei, T., Zhou, H., Wang, H., 2023. Co-adsorption mechanisms of Cd (II) and As (III) by an Fe-Mn binary oxide biochar in aqueous solution. Chemical Engineering Journal 466, 143199.

Yin, G., Song, X., Tao, L., Sarkar, B., Sarmah, A.K., Zhang, W., Lin, Q., Xiao, R., Liu, Q., Wang, H., 2020a. Novel Fe-Mn binary oxide-biochar as an adsorbent for removing Cd (II) from aqueous

solutions. Chemical Engineering Journal 389, 124465.
Yin, G., Song, X., Tao, L., Sarkar, B., Sarmah, A.K., Zhang, W., Lin, Q., Xiao, R., Liu, Q., Wang, H., 2020b. Novel Fe-Mn binary oxide-biochar as an adsorbent for removing Cd(II) from aqueous solutions. Chemical Engineering Journal 389, 124465. https://doi.org/10.1016/j.cej.2020.124465
Yuan, X., Suvarna, M., Low, S., Dissanayake, P.D., Lee, K.B., Li, J., Wang, X., Ok, Y.S., 2021. Applied machine learning for prediction of CO2 adsorption on biomass waste-derived porous carbons. Environmental Science & Technology 55, 11925–11936.
Zhang, H., Huang, H., Fang, Y., Cai, J., Lv, X., Wu, W., Gu, Q., Qian, R., Yu, K., Tang, K.H.D., 2025. Synthesis of magnetic biochar co-doped with sulfur, iron, and manganese via a novel modification method for simultaneous Cd and Pb remediation. Separation and Purification Technology 363, 132025.
Zhang, H., Xu, F., Xue, J., Chen, S., Wang, J., Yang, Y., 2020. Enhanced removal of heavy metal ions from aqueous solution using manganese dioxide-loaded biochar: Behavior and mechanism. Sci. Rep. https://doi.org/10.1038/s41598-020-63000-z
Zhang, J., Fu, K., Wang, D., Zhou, S., Luo, J., 2024. Refining hydrogel-based sorbent design for efficient toxic metal removal using machine learning-Bayesian optimization. Journal of Hazardous Materials 479, 135688.
Zhang, J., Ma, X., Yuan, L., Zhou, D., 2020. Comparison of adsorption behavior studies of Cd2+ by vermicompost biochar and KMnO4-modified vermicompost biochar. Journal of Environmental Management 256, 109959.
Zhang, L., Ren, Y., Xue, Y., Cui, Z., Wei, Q., Han, C., He, J., 2020. Preparation of biochar by mango peel and its adsorption characteristics of Cd(II) in solution. RSC Adv. https://doi.org/10.1039/d0ra06586b
Zhang, R., Liu, S., Lian, C., Yu, J., Lin, S., 2025. Machine Learning-Accelerated Design of High-Efficient Lithium Adsorbents for Salt Lake Brines. Angewandte Chemie 137, e202503644.
Zhang, W., Chen, R., Li, J., Huang, T., Wu, B., Ma, J., Wen, Q., Tan, J., Huang, W., 2023. Synthesis optimization and adsorption modeling of biochar for pollutant removal via machine learning. Biochar 5, 25.
Zhang, Y., Li, A., Liu, L., Duan, X., Ge, W., Liu, C., Qiu, G., 2023. Enhanced remediation of cadmium-polluted soil and water using facilely prepared MnO2-coated rice husk biomass. Chemical Engineering Journal 457, 141311.
Zhao, C., Zhang, J., Zhang, W., Yang, Y., Guo, D., Zhang, H., Liu, L., 2024a. Reveal the main factors and adsorption behavior influencing the adsorption of pollutants on natural mineral adsorbents: Based on machine learning modeling and DFT calculation. Separation and Purification Technology 331, 125706.
Zhao, C., Zhang, W., Zhang, Y., Yang, Y., Guo, D., Liu, W., Liu, L., 2024b. Influence of multivalent background ions competition adsorption on the adsorption behavior of azo dye molecules and removal mechanism: Based on machine learning, DFT and experiments. Separation and Purification Technology 341, 126810.
Zhao, Shuyan, Guo, J., Tang, Y., Zhou, Y., 2025. Applications of machine learning in heavy metal adsorption modeling: A review. Separation and Purification Technology 134168.
Zhao, Shilin, Liu, Q., Wang, Y., Wang, L., Zhang, J., Sun, Z., 2025. Machine Learning-Assisted Prediction of Mercury Removal Efficiency of Carbon-Based Adsorbents. Environmental Science & Technology 59, 17677–17687.

Data-driven machine learning models for guiding the preparation of Mn-modified biochar and predicting Cd adsorption

Weihan Wang[a,1], Ziqing Zhou[a,1], Jiarui Wang[a], Haoyu Cao[b], Bing Geng[a], Liangguo Luo[a], Jie Zhu[a], Changxiong Zhu[c], Xiangqun Zheng[a,*], Liyuan Liu[a,*]

[a]*Institute of Environment and Sustainable Development in Agriculture, Chinese Academy of Agricultural Sciences, Zhongguancun South Street, Beijing, 100081, China*

[b]*Agro-Environmental Protection Institute, Ministry of Agriculture and Rural Affairs, Tianjin 300191, China*

[c]*College of Environmental Science and Engineering, Hebei University of Science and Technology, Shijiazhuang, 050018, China*

[1] *contributed equally to this manuscript.*

**Corresponding author:*

Liyuan Liu, E-mail: liuliyuan@caas.cn□

Xiangqun Zheng, E-mail: zhengxiangqun@126.com;

Telephone: +86 (022)-82109567.

Abstract

Cadmium (Cd), a typical highly toxic heavy metal, poses serious risks to environmental safety and public health once it enters water bodies. Manganese-modified biochar (Mn-BC) can effectively remove Cd from wastewater. However, the need for complex batch experiments represents a major constraint on its development. The emergence of artificial intelligence provides a new approach to address this

problem. In this study, six machine learning (ML) models were developed to predict the Cd adsorption performance of Mn-BC, aiming to reduce the reliance on complex experimental procedures. Among the six models, the extra trees regressor (ETR) model achieved high prediction accuracy (test $R^2 = 0.970$; root mean square error (RMSE) = 12.982). The ETR model provided insights into the preparation of Mn-BC: the results of feature importance analysis revealed that the initial Cd concentration, biochar dosage, and manganese content were the main contributors to the model output. Additionally, the one-way partial dependence plots revealed that the optimal heating time in the biochar preparation process was 2 h, and the optimal manganese loading reached approximately 10%. To evaluate the practical applicability of the model, Mn-BC was prepared for conducting reverse validation of the ETR model, and the error between the predicted and experimental values was less than 17%. The results of characterization analyses, including X-ray photoelectron spectroscopy (XPS) and X-ray diffraction (XRD), revealed that Mn-BC adsorbed Cd mainly via coordination exchange and surface precipitation. This research not only presents an effective model for predicting adsorbent performance but also provides data-supported insights into the associations between complex preparation and adsorption conditions, thereby offering effective guidance and new insights for practical adsorbent fabrication.

Graphical abstract

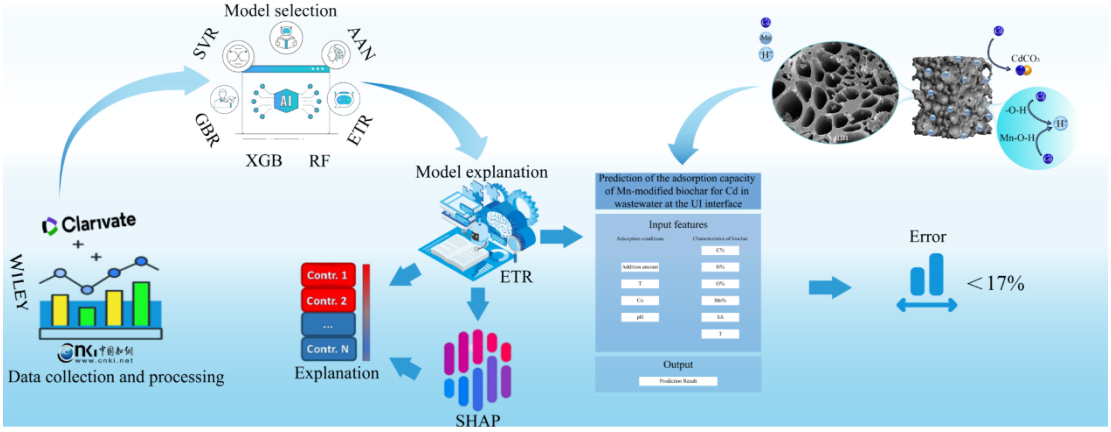

Keywords: Extra Trees Regressor, Manganese-modified Biochar, Adsorbent, Preparation Conditions, Cd

1. Introduction

Cadmium (Cd), a typical highly toxic heavy metal pollutant, is characterized by high toxicity even at low concentrations, nonbiodegradability, and easy migration and accumulation (Sun et al., 2023). Industrial production activities such as electroplating, battery manufacturing, and mining may produce wastewater that contains Cd (Jiang et al., 2024; Li et al., 2025). If not properly controlled, this wastewater can be absorbed by humans and ecosystems through drinking water, the food chain, and bioaccumulation, causing health problems such as kidney damage and bone metabolism disorders and posing serious threats to environmental and human health (Chen et al., 2022). Chemical precipitation readily causes secondary pollution (Xu et al., 2022), while membrane separation and electrochemical methods are costly and thus difficult to apply widely (J. Wang et al., 2023). Adsorption has received significant attention because it is simple to implement, broadly applicable, and easy to couple with existing treatment units (Tian et al., 2023).

Biochar is associated with abundant feedstock sources, a low preparation cost, and abundant surface functional groups, which render it an ideal carrier for adsorbents (Y. Wang et al., 2025). The oxygen-containing functional groups on the surface of biochar (such as carboxyl, hydroxyl, and phenolic hydroxyl groups) provide sites for complexation and ion exchange. However, pristine biochar exhibits limited active-site density, selectivity, and resistance to interference, especially under conditions of multi-ion coexistence or high ionic strength; thus, pristine biochar often fails to satisfy the demand for Cd removal (Mensah et al., 2025).

Loading metal oxides and hydroxides can significantly enhance the adsorption performance of biochar. For example, Fe–Mn bimetal-modified biochar can adsorb Cd(II) and As(III)/As(V) through synergistic mechanisms, including electrostatic attraction and ternary surface complexation (Yin et al., 2023). A mixture of industrial steel slag waste and ginkgo leaves was employed to prepare a novel magnetic adsorbent, which enhanced adsorbent recoverability while enabling the simultaneous adsorption of Cd(II) and As(V) (M. Wang et al., 2023). Mn-Fe bimetal sulfide-modified magnetic biochar derived from hardwood sawdust was synthesized via a stepwise activation–magnetization–sulfidation process, and its use improved the remediation of wastewater contaminated with Cd and Pb (H. Zhang et al., 2025). Among the various metal-modified biochar types, Mn-modified biochar (Mn-BC) exhibits an increased in situ Mn content on its surface, which increases the density of surface active sites and thus enhances its adsorption capacity (Wu et al., 2022).

Manganese oxide exhibits notable surface complexation. Cadmium can be effectively immobilized through coordination exchange and surface precipitation (for example, in 25 mL of a 100 mg/L Cd solution with a pH of 5.0, $Cd(OH)_2$ or $CdCO_3$ can be formed) (Yin et al., 2020) and synergistic interactions with oxygen-containing groups (Fan et al., 2020). Mn also alters the surface charge and acid–base properties of the material, which increases the adsorption stability over a wide range of pH values and enhances the resistance to interference from coexisting ions (Xiao et al., 2020).

Currently, the preparation of adsorbents relies mainly on a large number of experiments, especially batch tests, to determine the optimal preparation and adsorption

conditions. Although advanced tools such as density functional theory (DFT), molecular simulation, and the response surface methodology have been introduced, the preparation of adsorbents still depends on the experience of researchers and their understanding of material properties. Without experimental verification, the adsorption performance cannot be quantified accurately to identify the optimal preparation and adsorption conditions (W. Zhang et al., 2023). However, this method is time consuming and labour intensive, and the adsorbent may not provide the expected results (Shuyan Zhao et al., 2025). With the advent of artificial intelligence, emerging technologies such as machine learning (ML) can greatly reduce the complexity and workload of experimental procedures (Wang and Yao, 2025). ML facilitates the integration of multisource features (material structural parameters, chemical composition, process conditions, and water quality conditions) and facilitates the creation of input–performance maps in nonlinear and strongly coupled systems (Z. Wang et al., 2025). ML enables rapid prediction of the adsorption capacity and significantly reduces the cost of experimental iteration (Chen et al., 2025). After an ML model is established, the key features that determine Cd removal can be identified through feature importance analysis and SHapley Additive exPlanations (SHAP) analysis (Zhao et al., 2024a). ML can integrate the effects of multiple variables, thereby providing a more precise range, which can fulfil a certain guiding role in the design of adsorption materials (Li et al., 2026). Researchers have applied ML to reveal the effect of multivalent background ions (including Ca, K, Na, and Mg) on the adsorption capacity of natural mineral materials for azo dye molecules (Zhao et al., 2024b). By integrating advanced ML techniques

with interpretability tools, researchers have advanced the understanding of ammonia adsorption on biochar (Liu et al., 2025). To rapidly identify effective doping strategies for aluminium-based lithium adsorbents, ML has been employed to guide material screening (R. Zhang et al., 2025). ML models have been adopted to predict the adsorption capacity of arsenite (As(III)) and arsenate (As(V)) on different materials (R^2=0.987; RMSE=3.54) (Huang et al., 2025).

This study focuses on the preparation process of Mn-BC and introduces the preparation conditions, elemental content, pore structure, and other key influencing indicators of Mn-BC. An ML model is established to predict the actual adsorption performance of biochar before its preparation and to provide data-supported guidance for adsorbent preparation to address Cd^{2+} pollution in the target water body, thereby providing directions for reverse design of adsorbents. The design concept of Cd biochar adsorbents is shifted from material preparation–performance testing to customized design of adsorption materials for the target water body.

In this study, ten key features related to the preparation conditions, material properties, and adsorption environment of Mn-BC were selected to predict its Cd adsorption capacity. This study aimed to (1) identify the optimal prediction model through comparative evaluation analysis; (2) quantify the effects of input variables on adsorption performance via feature importance analysis and identify key predictive factors; (3) partially analyse the preparation conditions for biochar; and (4) guide practical experiments with the optimal prediction model, evaluate the prediction performance, and examine possible adsorption mechanisms. Via the use of a data-

driven ML model, this study provides new insights for the rational design and optimization of efficient biochar adsorbents and helps overcome the limitations of traditional methods.

2. Materials and methods

2.1 Data collection

As shown in Fig. 1, the dataset in this study was collected from the Web of Science, Wiley Online Library, and China National Knowledge Infrastructure (CNKI) databases. The publication period was limited to the 2014–2025 range. To enhance the completeness and reproducibility of the literature search, the following search string was adopted: TS = ("Mn" OR "manganese" OR "manganese oxide" OR "manganese-modified" OR "manganese-loaded") AND ("biochar" OR "modified biochar") AND ("cadmium" OR "Cd") AND ("adsorption" OR "removal"). The initial search records were screened according to predefined inclusion and exclusion criteria. Studies were included when they satisfied the following criteria: (i) Mn-BC was employed as the adsorbent; (ii) Cd(II) adsorption was investigated in aqueous solutions; (iii) the adsorption capacity or sufficient data for calculating the adsorption capacity were reported; and (iv) data for the selected feature variables were available without missing values. Studies involving non-Mn-BC, mixed contaminants without separable Cd adsorption data, soil-only immobilization experiments, review articles, duplicated publications, or records with missing key variables were excluded .

Duplicate records were first removed on the basis of the title, DOI, and author information. The title and abstract of the remaining articles were then reviewed,

followed by full-text evaluation. When the same data appeared in both figures and tables, tabulated values were preferentially chosen. With respect to data reported only in figures, WebPlotDigitizer was applied for extraction. After duplicate records and incomplete entries were removed, 27 papers were ultimately retained, yielding 1,016 valid data records (The DOI of the literature and the journal were listed in Table S3).

The input variables were selected to cover the major stages from biochar preparation to Cd adsorption. Specifically, the pyrolysis time (t) represents the preparation conditions; the adsorption temperature (T), biochar dosage, solution pH, and initial Cd concentration (C0) represent the adsorption conditions; and the carbon content (C%), oxygen content (O%), hydrogen content (H%), Mn loading percentage (Mn%), and specific surface area (SA) represent the physicochemical properties of Mn-BC. These ten variables were selected because they are frequently reported in the literature and are directly related to the biochar structure, Mn modification, surface chemistry, and Cd adsorption behaviour.

2.2 Model training

All the algorithms and functions chosen in this study were implemented in Python 3.12.7. The main software packages include pandas 3.0.3, numpy 1.26.4, matplotlib 3.10.9, seaborn 0.13.2, scikit-learn 1.7.2, bayesian-optimization 3.0.1, SHAP 0.49.1, and XGBoost 3.0.5. Six ML algorithms were selected for model development, namely, random forest (RF), extra tree regressor (ETR), gradient boosting regressor (GBR), extreme gradient boosting (XGB), artificial neural network (ANN), and support vector regression (SVR) models (Fig. 1). The coefficient of determination (R^2) was applied to

evaluate the goodness of fit of the models (Shilin Zhao et al., 2025). The differences between the observed and predicted values were quantified on the basis of the RMSE, mean absolute error (MAE), and mean bias error (MBE) (Jie Li et al., 2024).

$$R^2 = 1-\frac{\sum_{i=1}^{n}(y_i-\hat{y}_i)^2}{\sum_{i=1}^{n}(y_i-\bar{y})^2} \quad (1)$$

$$RMSE = \sqrt{\frac{1}{n}\sum_{i=1}^{n}(\hat{y}_i-y_i)^2} \quad (2)$$

$$MAE = \frac{1}{n}\sum_{i=1}^{n}|\hat{y}_i-y_i| \quad (3)$$

$$MBE = \frac{1}{n}\sum_{i=1}^{n}(\hat{y}_i-y_i) \quad (4)$$

where y_i denotes the actual observed value, $\hat{y}_i$ denotes the predicted value, $\bar{y}$ denotes the mean of the observed values, and n denotes the sample size.

2.3 Model interpretation

Through the use of the prebuilt frameworks and libraries provided by scikit-learn, ML modelling (evaluation, interpretation, and application) was conducted. In the dataset, 80% of the data were randomly assigned to the training set, and the remaining 20% were employed to validate the final model. During Bayesian hyperparameter optimization, fivefold cross-validation was applied to the training set containing 80% of the data; four folds were used for training, and one fold was adopted for validation (Zhang et al., 2024). SHAP analysis was employed to interpret feature importance and to help determine the contribution of each feature to the model predictions (Yang et al., 2021). One-way partial dependence analysis was conducted to examine how each input feature affected the output variable, and two-way partial dependence analysis was used to analyse the interaction effects between different features (Yuan et al., 2021).

2.4 Experimental verification under the guidance of machine learning models

Biochar was prepared from corn straw through pyrolysis. Briefly, the raw biomass was washed with deionized water, dried at 50 °C, ground, and sieved through a 20-mesh screen. The dried biomass was then pyrolyzed at 250 °C for 2 h in an oxygen-free atmosphere at a heating rate of 10 °C min^{-1}. The obtained biochar was denoted as BC.

Mn-BC was prepared via the use of a coprecipitation method. Briefly, 1 g of BC was added to 100 mL of a 0.1 mol/L $KMnO_4$ solution, corresponding to a solid-to-liquid ratio of 10 g/L. The suspension pH was adjusted to 10 using a 0.1 mol/L NaOH solution. After ageing at room temperature for 3 h, the suspension was centrifuged, and the precipitate was washed several times with deionized water until the supernatant became neutral. Finally, the obtained Mn-BC was dried at 35 °C overnight.

The morphology and elemental distribution of the samples were characterized via scanning electron microscopy coupled with energy-dispersive spectroscopy (SEM–EDS; TESCAN MIRA LMS). The SA and pore structure were determined through the Brunauer–Emmett–Teller (BET) method (Micromeritics ASAP 2460). The crystalline phases were analysed by X-ray diffraction (XRD; Rigaku SmartLab SE). The surface elemental composition and chemical states were analysed via X-ray photoelectron spectroscopy (XPS; Thermo Scientific ESCALAB 250Xi). The surface functional groups were identified through the use of Fourier transform infrared spectroscopy (FTIR; Thermo Scientific Nicolet iS20). The elemental composition was determined with an elemental analyser (EA; Elementar Unicube), and the Cd concentration was measured via inductively coupled plasma–mass spectrometry (ICP–MS; Agilent 7800 ICP–MS).

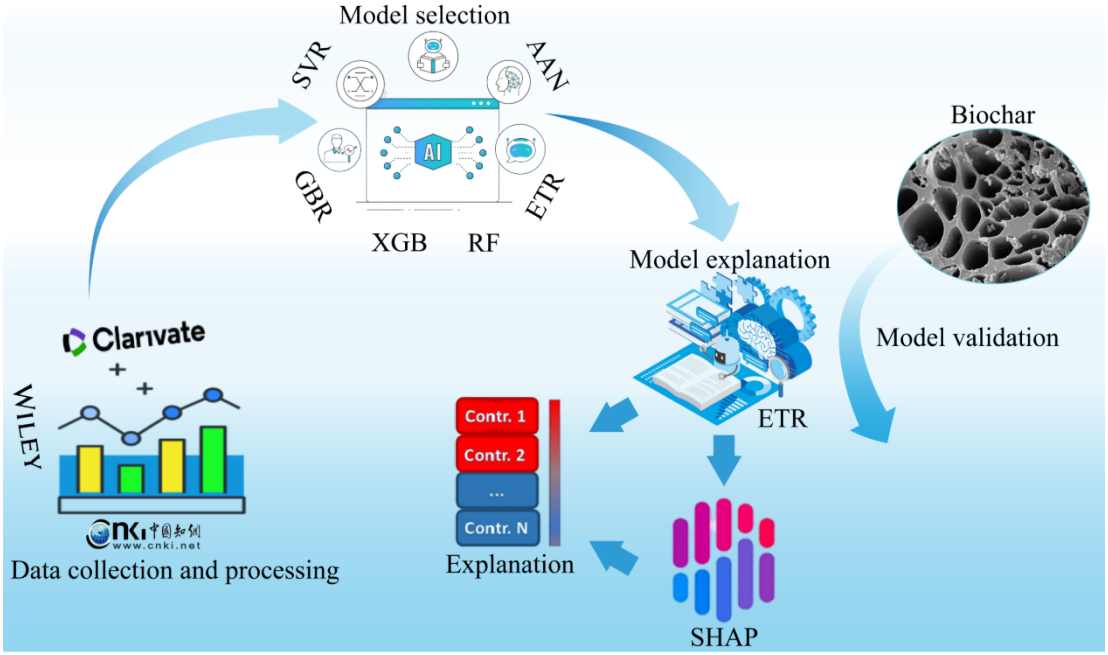

Fig 1. The process of model establishment, evaluation, interpretation and application.

3. Results and discussion

3.1 Statistical analysis of datasets

The different physicochemical properties of biochar and the adsorption conditions are shown in Fig. 2. The elemental composition of biochar, including the contents C, of H, O, and Mn, is shown in Fig. 2a. The C content was generally high, confirming that carbon constituted the main structural framework of biochar. In contrast, the H content remained relatively low, which should not be interpreted only from its absolute mass fraction. For biochar, the atomic H/C ratio is a meaningful indicator of aromaticity, degree of carbonization, and structural stability. A lower H/C ratio usually reflects greater dehydration and dehydrogenation during pyrolysis, accompanied by the formation of more condensed aromatic carbon structures. Conversely, a higher H/C ratio indicates a lower degree of carbonization and greater retention of aliphatic or hydrogen-containing structures. Therefore, the variation in the H content may indirectly

reflect changes in the H/C ratio and the evolution of biochar aromaticity and surface chemistry (Xiao et al., 2016). This structural evolution is closely related to Cd adsorption because excessive carbonization may reduce the number of surface functional groups, whereas moderate carbonization can preserve oxygen- and hydrogen-containing functional groups that contribute to Cd complexation and coordination (J. Zhang et al., 2020). A higher O content in biochar helps increase the abundance of oxygen-containing functional groups on its surface (such as carboxyl and hydroxyl groups), thereby enhancing complexation and ion exchange with Cd^{2+}; therefore, the O content in most biochars is approximately 20% (Sun et al., 2022). As a dopant element, the content of Mn was relatively low, mostly less than 20%. However, the Mn content is likely among the key factors influencing the adsorption of Cd^{2+} by biochar (Wu et al., 2022).

The environmental factors during Cd^{2+} adsorption by biochar, including the biochar dosage, initial solution pH, and adsorption temperature, are shown in Fig. 2b. The amount of added biochar is usually small (< 10 g/L), which might occur because excessive addition of biochar can lead to waste, as the adsorption capacity of biochar is not solely determined by the amount of added biochar but also depends on factors such as the pH (Qu et al., 2023). Because Cd^{2+} precipitates under alkaline conditions, the adsorption solution is generally acidic (< 7), and in real-world Cd^{2+}-containing wastewater, the solution pH is lower than 8. The adsorption temperature is approximately 25 °C, which aims to simulate the ambient temperature in practical adsorption processes (Kong et al., 2024).

The SA of biochar and the initial Cd^{2+} concentration are shown in Fig. 2c. The SA was correlated with the adsorption capacity of biochar; notably, a relatively large surface area likely provides more active sites and pore channels, thereby promoting the physical adsorption and chemical binding of metal ions (J. Wang et al., 2025). Different Cd^{2+} concentration gradients result in distinct concentration differences, which in turn affects the adsorption capacity of biochar (Kong et al., 2023b).

As shown in Fig. 2d, the use of different pyrolysis times affects the adsorption performance of biochar by altering its functional groups. At shorter pyrolysis times, the produced biochar retains more functional groups. With increasing pyrolysis time, the aromaticity of biochar increases, whereas the number of oxygen-containing functional groups decreases, which reduces the number of adsorption sites on the surface of biochar and thus attenuates its adsorption performance (Jishuo Li et al., 2024). Overall, the elemental composition, SA, and external environmental conditions (such as the pH, temperature, and concentration) jointly influence the adsorption behaviour and mechanism of Cd^{2+} on the surface of Mn-BC.

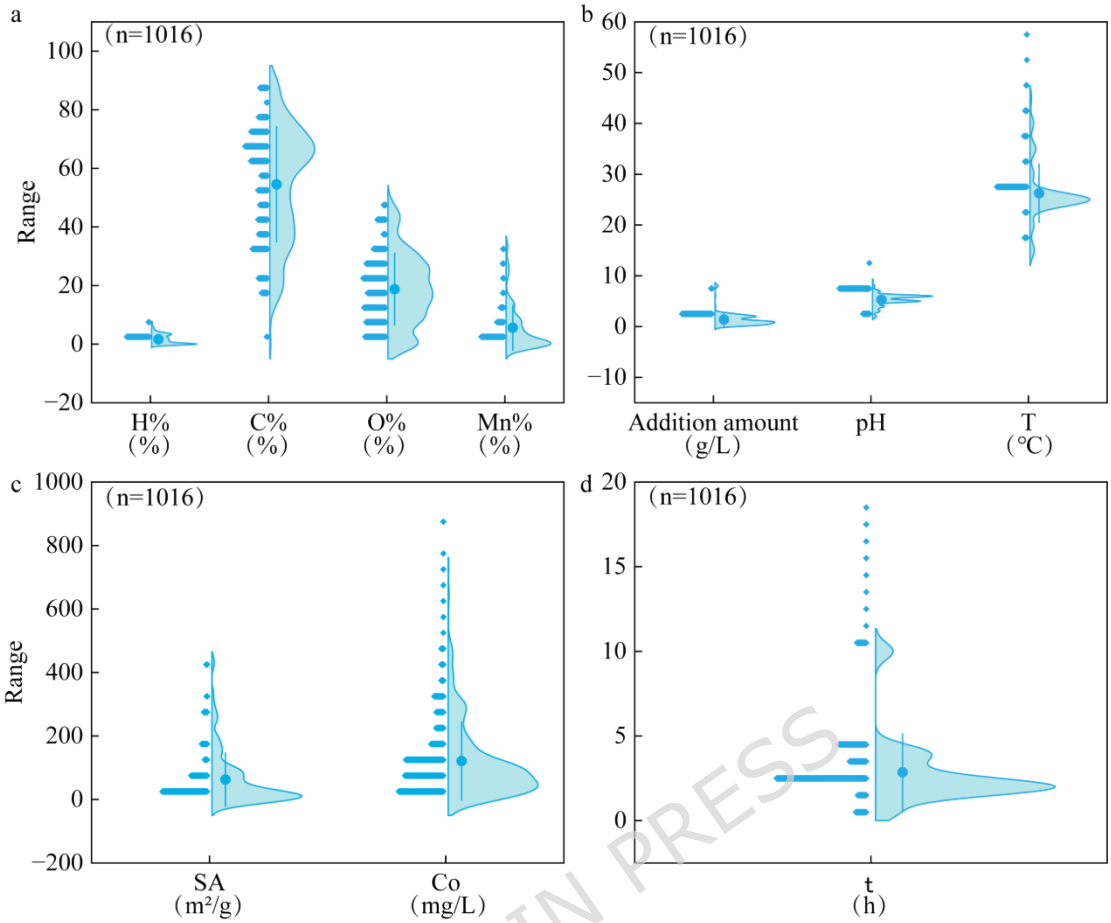

Fig 2. Presents boxplots of each parameter: H%, C%, O%, and Mn%, (a); Addition Amount, pH,T (b); and SA, Co (c); and t (d).

3.2 Pearson correlation coefficient analysis

Pearson's correlation analysis among different variables was conducted to examine the relationships between feature parameters, and the results are shown in Fig. 3. As shown in Fig. 3, significant correlations were observed among most parameters, suggesting potential coupling relationships between the adsorption conditions and the physicochemical properties of biochar.

Ce was significantly correlated with most of the variables, indicating that Cd^{2+} adsorption by Mn-BC was associated with both the adsorption conditions and biochar properties. Specifically, H%, O%, Mn%, and Co were significantly positively correlated with Ce, suggesting that biochars with higher contents of hydrogen- and

oxygen-containing components, higher Mn loadings, and higher initial Cd^{2+} concentrations exhibit higher adsorption capacities. The positive correlation between Co and Ce may be related to the increased concentration gradient at higher initial Cd^{2+} concentrations, which could influence the adsorption performance of biochar (Lian et al., 2020).

C% ($p<0.001$) and H% ($p<0.001$) in the elemental composition of biochar were strongly significantly correlated with t, indicating that variations in the pyrolysis time were associated with changes in H% during biomass pyrolysis and may reflect differences in the abundance of hydrogen-containing functional groups. C% was significantly negatively correlated with H% ($0.01<p<0.001$), O% ($p<0.001$), and Mn% ($p<0.001$), suggesting that biochars with higher C% values contained lower contents of hydrogen- and oxygen-containing components and lower Mn contents. The SA was strongly correlated with most other factors, and these correlations were mainly negative, indicating that a greater SA value was generally associated with lower adsorption performance in this dataset. This result should not be interpreted as a direct adverse effect of the SA itself but may reflect the coupled influence of the preparation conditions. Previous studies have revealed that biochars with higher SA values do not necessarily exhibit higher Cd^{2+} adsorption capacities because Cd^{2+} adsorption by biochar is often governed by chemical interactions such as ion exchange, surface complexation, and precipitation rather than the physical surface area alone (Dai et al., 2021; L. Zhang et al., 2020). This relationship may be related to differences in the preparation process. For example, high pyrolysis temperatures can increase the SA of

biochar while reducing the number of H- and O-containing components and surface functional groups, which may reduce the contribution of chemically active sites to Cd^{2+} adsorption.

Overall, the elemental composition of biochar (C%, O%, Mn%, and SA) and the initial environmental conditions during adsorption jointly affect Cd^{2+} adsorption by Mn-BC.

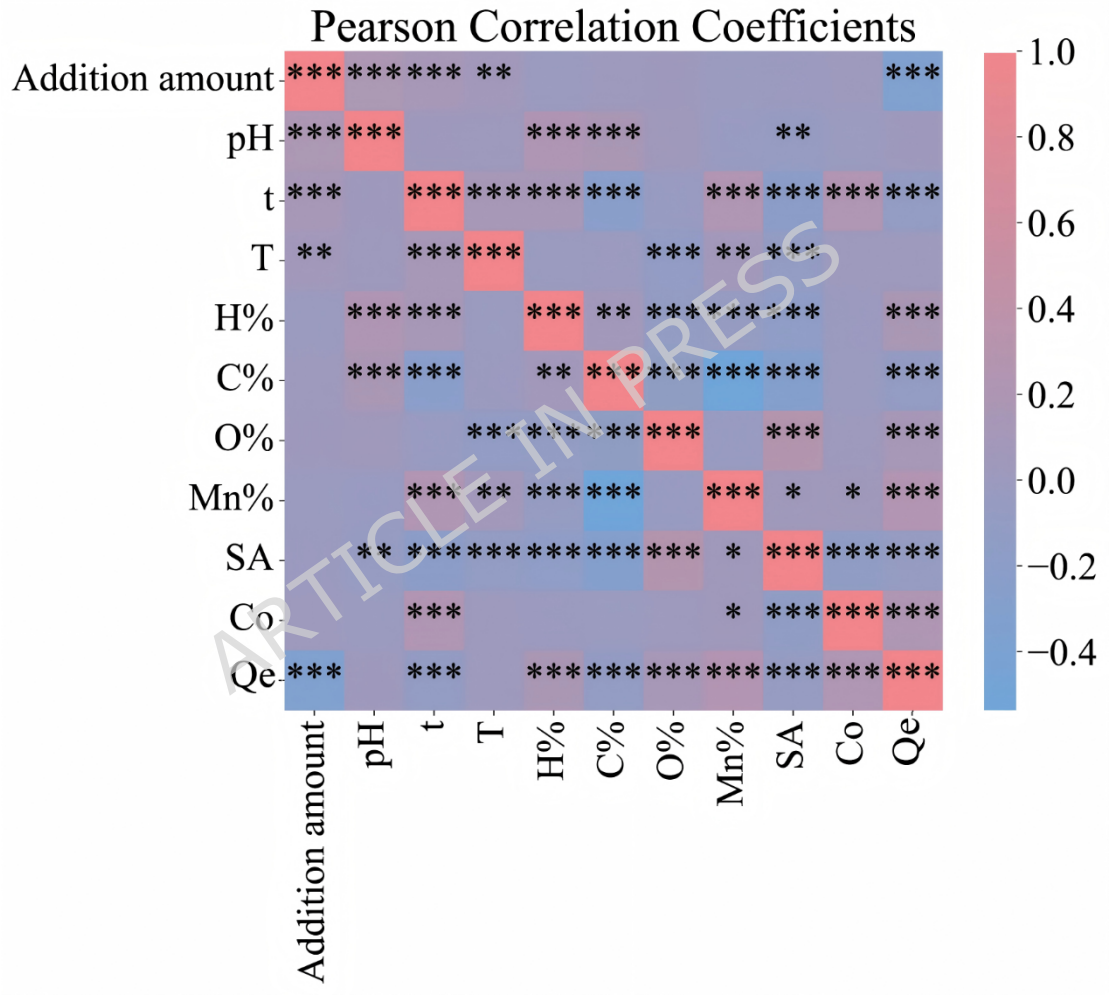

Fig 3. Pearson correlation heatmap with significance levels (the color intensity indicates the strength of correlation between variables, and * significant ** extremely significant *** extraordinarily significant).

3.3 Model prediction

The prediction results of Cd^{2+} adsorption performance obtained with different ML models are shown in Fig. 4. As shown in Fig. 4a–f, the prediction accuracy clearly varied among the models. The ETR model achieved the best performance, with the highest R^2 value (0.970) and the lowest RMSE value (12.982). Compared with the RF and boosting models (GBR and XGB), the ETR model introduces a higher degree of randomness in feature splitting and sample selection, which effectively reduces model variance and avoids overfitting. As a result, this model attained greater stability and generalization for the test set and an improved ability to capture complex nonlinear relationships.

Among the ETR, ANN, and SVR models, the ANN model can simulate highly complex input–output relationships and performs better than linear or tree-based models do (Chellappa et al., 2021). The SVR model was solved globally through the use of kernel techniques, dual transformation, and the sequential minimal optimization (SMO) algorithm, which enables it to gradually approximate complex nonlinear relationships, similar to the GBR model but in a more concise form (Huang et al., 2022). The prediction performance of the ANN and SVR models was worse than that of the ETR model. In terms of R^2, RMSE, MAE, and MBE, the ETR model outperformed the other models.

Significance analysis was conducted for the different models (Fig. S2). Although the difference between the RF and ETR models was not significant, in comparison, the ETR model performed the best among all the algorithms (R^2 = 0.970; RMSE = 12.982; Table 1), suggesting satisfactory prediction performance in resolving high-dimensional

nonlinear relationships and complex feature interactions. Therefore, subsequent analyses were conducted on the basis of the ETR model, including feature importance and interpretability analyses, to identify the key variables contributing to model predictions of the adsorption performance of Mn-BC and to clarify their underlying mechanisms.

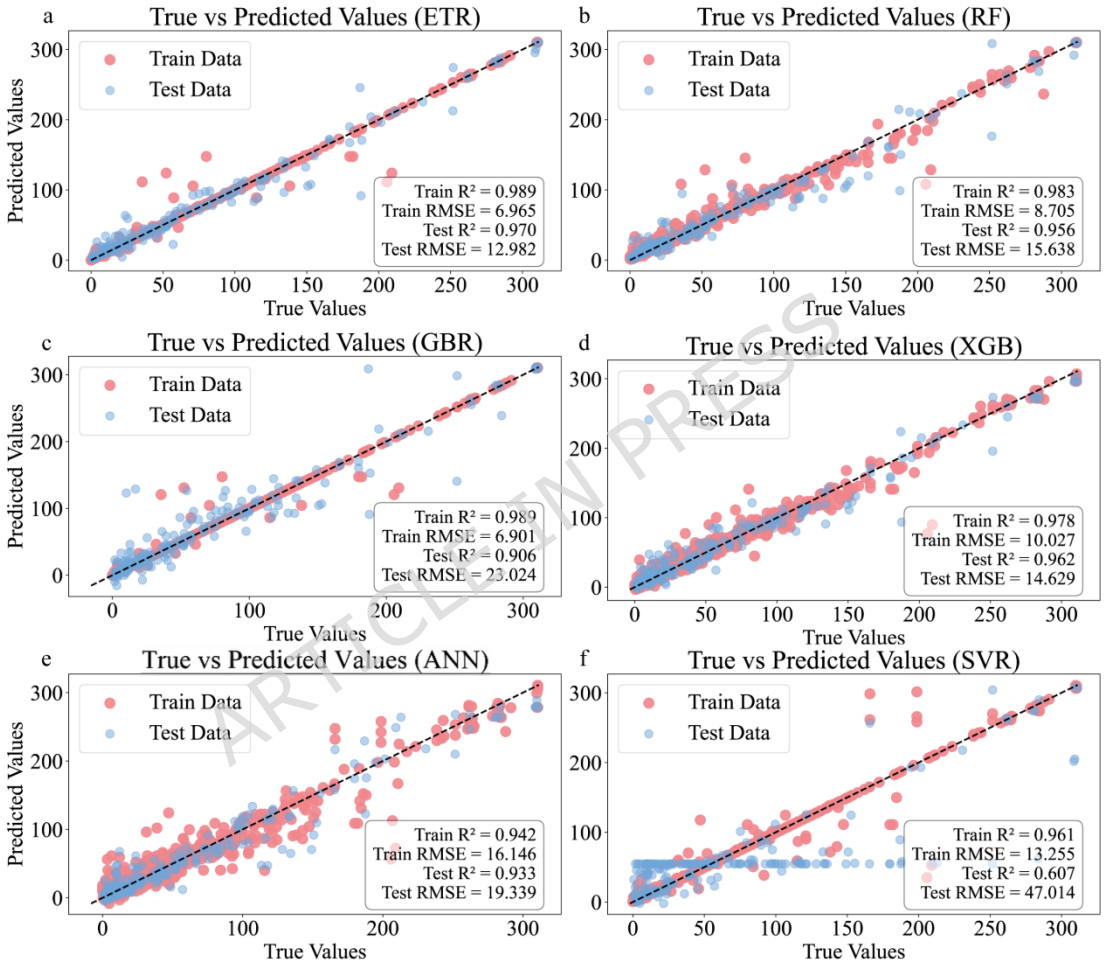

Fig 4. Prediction plots of the ETR (a), RF (b), GBR (c), ANN (e), and SVR (f) models.

Table 1. R^2, RMSE, MAE, and MBE of the ETR, GBR, RF, XGB, ANN, and SVR models.

	R^2		RMSE		MAE		MBE	
	Train	Test	Train	Test	Train	Test	Train	Test
ETR	0.989	0.970	6.965	12.982	0.862	6.498	0.000	0.097
RF	0.983	0.956	8.705	15.638	3.604	8.475	0.227	-1.181

GBR	0.989	0.906	6.901	23.024	0.861	12.200	-0.200	-5.978
XGB	0.978	0.962	10.027	14.629	5.296	9.209	-0.003	-0.585
ANN	0.942	0.933	16.146	19.399	9.183	12.512	-1.823	-2.964
SVR	0.961	0.607	13.255	47.014	2.886	0.607	-0.054	-6.179

3.4 Model fitting and feature importance analysis

The learning curves, residual plots, and feature importance results of the ETR model are shown in Fig. 5, which are used to validate model stability and quantify the contributions of key features. As shown in Fig. 5a–b, with increasing training set size, the prediction accuracy increased notably: the test-set R^2 value first gradually increased and then stabilized, eventually exceeding ~0.9, whereas the RMSE continuously decreased and remained low. This trend suggests that with sufficient samples, the ETR model effectively learned complex feature relationships and achieved suitable generalizability and robustness.

As shown in Fig. 5c, the residuals were randomly distributed around zero, and the residual ranges for the training and test sets were similar. No systematic bias was observed, which indicates that the model yields a good fit (Nandi et al., 2025). These results confirmed the reliability of the ETR model for predicting Cd^{2+} adsorption performance.

The feature importance results obtained with the different methods, including the mean absolute SHAP value (MAS), embedded feature importance (EFI), and permutation feature importance (PFI), are shown in Fig. 5d–f (Neubauer et al., 2024). The three methods yielded highly consistent results, and all the results indicated that Co and Mn% were the main predictors contributing to the prediction of the adsorption capacity. This result was likely due to the relatively high manganese content, which

increased the number of surface active sites and thereby promoted the binding of Cd^{2+}, whereas the notable effect of Co suggested that the initial concentration gradient was among the key forces driving adsorption. This occurred mainly because a relatively large difference in concentration could enhance Cd^{2+} transport, thereby improving the adsorption performance of Mn-BC (Fan et al., 2020). The variables of the addition amount, H%, and O% followed in importance. Although C%, SA, pH, and T also contributed to the observed increase, their importance was relatively low.

Overall, Co and Mn% were the primary factors governing the adsorption performance of Mn-BC.

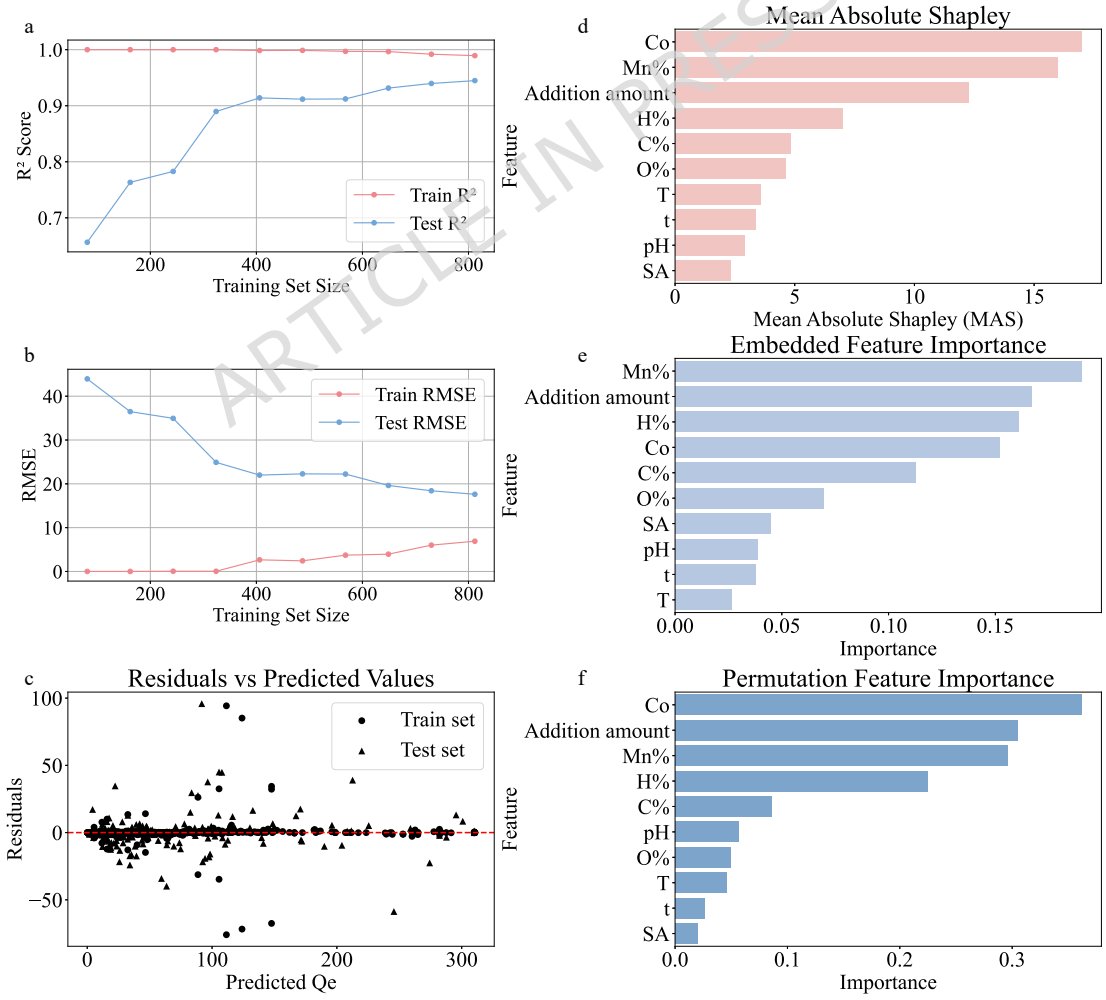

Fig 5. Learning curves of R^2 (a) and RMSE (b); Prediction residual plot (c); PFI (d) and

EFI (e) feature importance analysis; MAS values of feature importance (f).

3.5 Model SHAP analysis and one-way partial dependence analysis

As shown in Figure 6a, there was a significant difference in the distribution of the SHAP values for the input features. The average absolute SHAP values of Co and Mn% were the highest, indicating that they contributed the most to the model predictions. The SHAP values of Co were mainly positive, suggesting that the initial concentration contributed positively to the adsorption capacity. This greater contribution may be related to the adsorption mechanism driven by the concentration gradient in the solution. The positive contribution of the positive SHAP values of Mn% suggested that a higher Mn% value was associated with higher predicted adsorption capacity of the binding sites on the surface of biochar, thereby strengthening its complexation ability. The variables of the addition amount and H% ranked next in importance. The distribution of SHAP values of the addition amount was mainly negative, indicating that an excessive dosage, while reducing Cd^{2+} in water, also decreased the adsorption capacity per unit mass of biochar (Kong et al., 2023a). H% yielded a positive effect, mainly because H% was closely related to surface functional groups; notably, a higher H% value increased the abundance of hydrogen-containing functional groups on the surface of biochar, thereby providing more binding sites for Cd^{2+} (H. Zhang et al., 2025). O%, SA, and t also generated notable effects, indicating that the physicochemical properties of biochar and the adsorption environment played supportive roles in driving Cd^{2+} adsorption by biochar.

The one-way partial dependence plots of the main features are shown in Fig. 6b to explain their effects. With increasing adsorbent dosage, the theoretical adsorption

capacity per unit mass of biochar first decreased rapidly but then stabilized. The partial dependence plots suggested a positive marginal association with the adsorption performance, which might be attributed to the change in hydrogen-containing functional groups (H. Zhang et al., 2020); biochar achieved relatively satisfactory adsorption when the H% value reached approximately 5%. Both O% and Mn% first increased but then decreased, indicating that moderate contents were most favourable for Cd^{2+} adsorption. Excessive Mn loadings may lead to Mn oxide aggregation and a reduced utilization efficiency of active Mn sites, thereby limiting further improvement in the Cd adsorption performance (H. Zhang et al., 2020); the adsorption performance was better when Mn% and O% reached approximately 10% and 35%, respectively. The SA first increased but then decreased, possibly because achieving an excessively high surface area requires a longer carbonization time. For $t > 4$ h, the adsorption performance decreased considerably. Therefore, a lower SA could help facilitate the retention of surface functional groups and thus enhance adsorption. The pyrolysis time should be < 4 h. Although the SA value increased, many binding sites might be lost. The one-way partial dependence plots of the pH, T, and Co indicated that the adsorption capacity increased gradually as the values of these variables increased (Fig. S1).

Co and Mn% were the most influential in model prediction, while the C, H, and O ratios and pore-structure parameters also participated in regulating the adsorption behaviour. The combination of SHAP and partial dependence plot analyses not only supported the reliability and interpretability of the model but also provided a theoretical basis for clarifying the key mechanisms underlying Cd^{2+} adsorption by biochar.

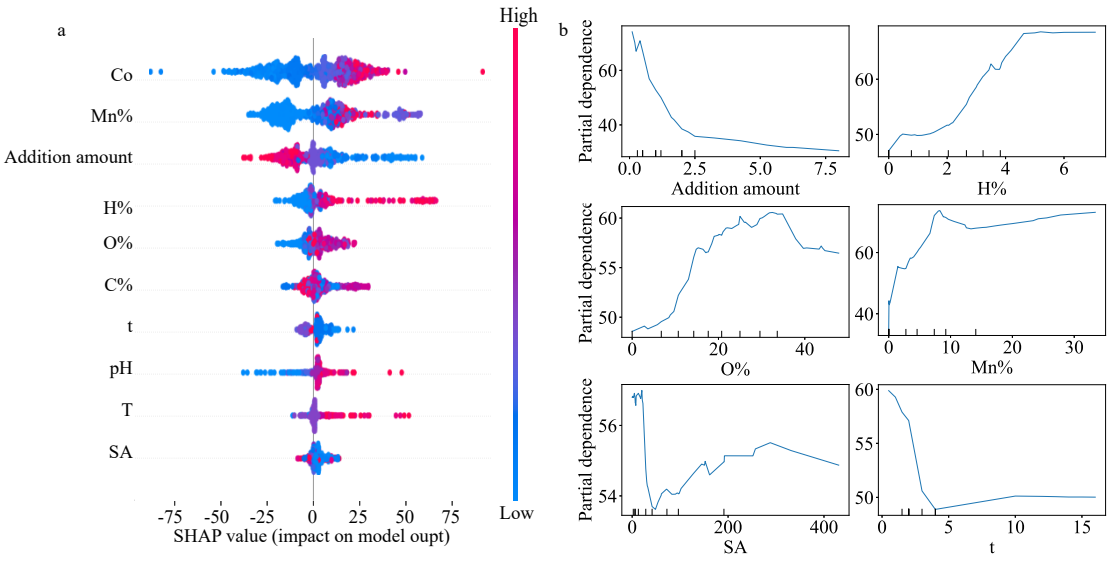

Fig 6. SHAP values of feature importance (a); The one-way partial dependence plot of each input feature in the ETR model (b).

3.6 Two-way partial dependence analysis

To clarify the effect of loading and the role of Mn in biochar, two-way partial dependence plots were created to analyse how different factors interact with Mn%. The bivariate interaction effects between the Mn-doping content (Mn%) and other key features (Co, pH, T, C%, H%, O%, SA, t, and addition amount) on the Cd^{2+} adsorption performance are shown in Fig. 7. The multiple influences of the predicted adsorption capacity under different parameter combinations are shown in Fig. 7a–i.

As shown in Fig. 7a, the interaction between Co and Mn% was significant. When Mn% was low, the adsorption capacity increased notably with increasing Co, whereas in the high-Mn% region, the positive effect of Co gradually weakened. This result indicates that under high-doping conditions, the number of Mn-provided surface reactive sites was close to saturation. Thus, increasing the initial concentration further yielded a limited promotional effect. As Mn% continuously increased, the adsorption

capacity first decreased but then increased, possibly because a higher Mn% value promoted metal aggregation on the surface of biochar and thus reduced the number of available binding sites. The combined effect of the pH and Mn% is shown in Fig. 7b, indicating that the positive effect of Mn doping was greatest under near-neutral conditions (pH: 6–7) and that a Mn content of approximately 10% resulted in relatively satisfactory adsorption performance.

The interactive effects of the temperature (T) and the elemental composition of biochar (C%, H%, and O%) with Mn% are shown in Fig. 7c–f. With increasing temperature, the overall adsorption performance improved, and biochar with higher Mn% values exhibited better Cd^{2+} removal at increased temperatures. This result indicates that the adsorption process is endothermic, which is consistent with the findings of previous studies (Yin et al., 2023). When C% ranged from 50–75%, positive synergy with Mn was observed, indicating that a higher degree of carbonization and metal doping jointly enhanced Cd^{2+} complexation. When Mn% reached approximately 10%, increasing H% improved the adsorption performance of biochar, which is likely related to the presence of hydrogen-containing functional groups on the surface of biochar. The changes in O% indicated that under both low- and high-Mn% conditions, O contents ranging from 15–40% are beneficial for Cd^{2+} adsorption, which might be associated with different Mn valence states (Liu et al., 2023).

As shown in Fig. 7g–i, the SA, t, and addition amount also exhibited significant interaction effects with Mn%. When the SA and Mn% were low, the adsorption capacity increased. Reducing the reaction time also improved the adsorption

performance, which might be attributed to the preservation of surface functional groups. The adsorption performance was better at a dosage of approximately 1 g/L.

Overall, the Cd^{2+} adsorption performance was controlled by Mn doping and multiparameter synergy. Increasing Mn% significantly amplified the positive effects of environmental and structural factors (such as the pH, temperature, and SA). However, an excessively high doping level could cause active-site saturation and aggregation effects, thereby limiting further improvement. A Mn content of approximately 10% promoted Cd^{2+} adsorption by biochar. These results confirm the key role of Mn doping in regulating Cd^{2+} adsorption by biochar.

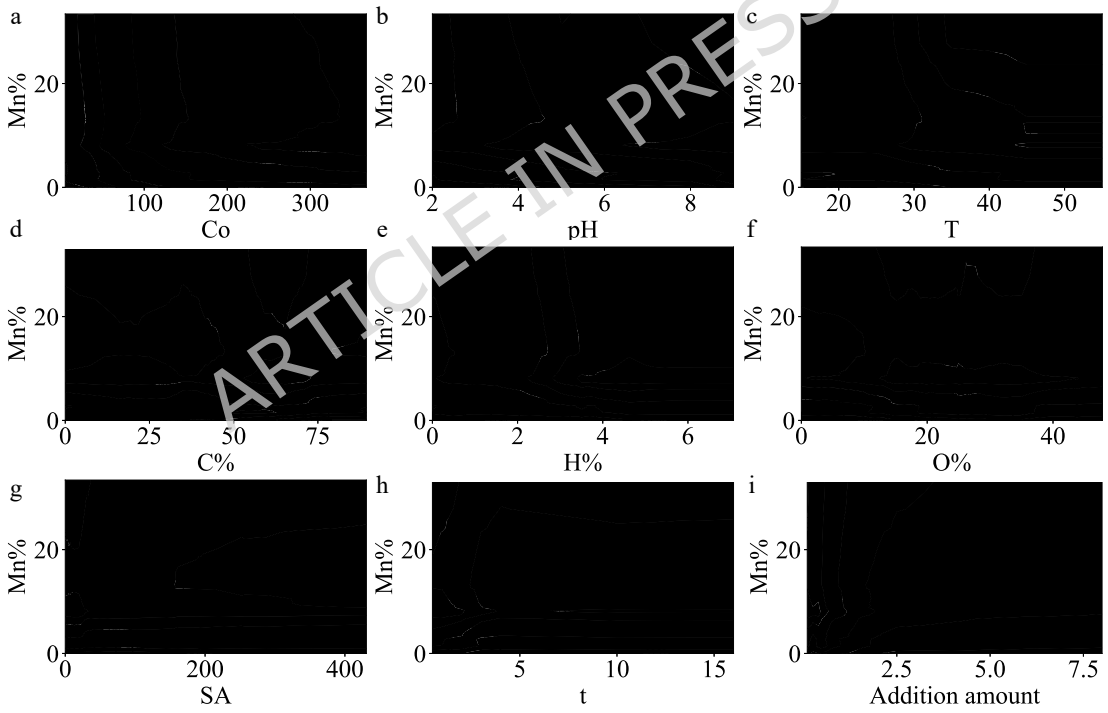

Fig 7. Two-way partial dependence plot of each input feature in the ETR model.

3.7 Experimental verification

To validate the model performance, rice husk biochar was modified with potassium permanganate under the guidance of the ETR model (Table S1). Under

different experimental conditions, the error between the actual performance of Mn-BC and the predicted performance was less than 17% (Table 2). This result indicates that the ETR model accurately predicted the adsorption performance of Mn-BC and provided effective guidance for its preparation.

Table 2. The predicted values output by the model and the actual adsorption capacity.

Predicted value	Actual adsorption capacity	Error
81.366	94.840	16.559
108.243	97.047	-10.343
84.280	95.371	13.160

3.8 SEM–EDS analysis

To validate the model performance, rice husk biochar was modified with potassium permanganate to obtain BC and Mn-BC. The micromorphology and elemental distribution of Mn-BC before and after Cd^{2+} adsorption are shown in Fig. 8. The surface structure of the pristine biochar is shown in Fig. 8a. At 5 μm, the biochar exhibited a three-dimensional porous network with a relatively uniform pore distribution and interconnected pore walls, forming a rich pore channel system. This structure facilitated rapid diffusion and mass transfer of Cd^{2+} in solution and provided sufficient contact interfaces for adsorption (Liu et al., 2022). The structures of Mn-BC and biochar after Cd adsorption are shown in Fig. 8b–c. Compared with the data in Fig. 8a, obvious precipitated substances were observed, indicating that Mn was successfully loaded onto the surface of biochar (the elemental maps in Fig. 8h–i and the EDS spectra also support this finding). These features were clearer at 500 nm. As shown in Fig. 8d–f, more precipitates occurred in the pore channels, which was likely due to successful Mn loading and Cd adsorption via surface precipitation. Moreover, the presence of Mn and

Cd in Fig. 8h–i confirmed the successful capture of Mn and Cd on the surface of biochar. The increased amounts of precipitates suggested an effective Mn content on the surface of biochar and within the pores, and after Cd^{2+} adsorption, select particles likely formed Cd–Mn complexes or precipitates with Cd^{2+}. This finding in turn indicates that Mn-BC adsorbed Cd^{2+} through chemisorption and surface reactions. The EDS spectra confirmed the presence of C, O, Mn, and Cd in the samples, and the characteristic Cd peak after adsorption indicated that Cd^{2+} was adsorbed on the surface of Mn-BC. Overall, the combined SEM and EDS results confirmed that Mn was successfully loaded onto the surface of biochar and enabled efficient capture of Cd^{2+}.

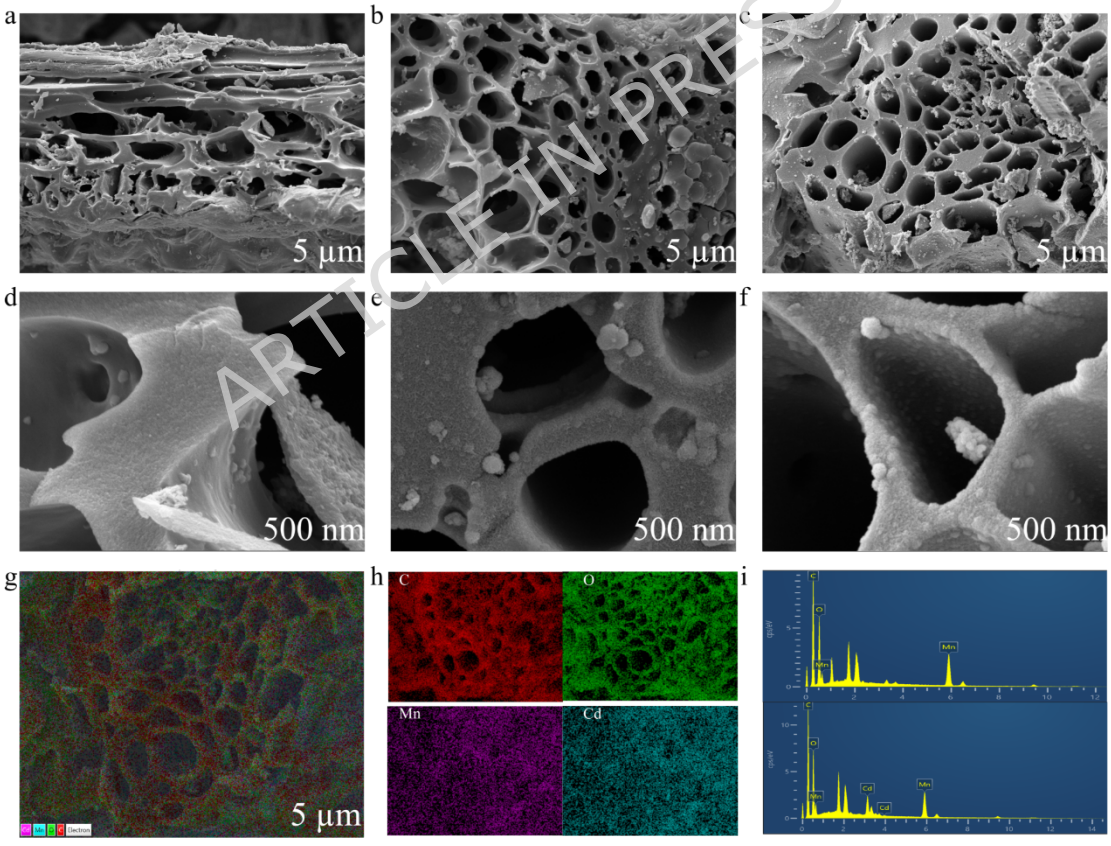

Fig 8. 5 μm scanning electron microscope images of BC (a), Mn-BC (b), and Cd-Mn-BC (c); 500 nm scanning electron microscope images of BC (d), Mn-BC (e), and Cd-Mn-BC (f); EDS mapping:C, O, Mn, Cd elemental distribution of the Cd-Mn-BC (g□

h); EDS spectrum of BC-Mn-BC (i).

3.9 Performance and mechanistic analysis

To investigate the Mn-BC adsorption mechanism, the biochar samples before and after adsorption were characterized. The adsorption capacity and removal efficiency of Mn-BC at different initial concentrations and dosages are shown in Fig. 9a. At a dosage of 1 g/L, Mn-BC achieved a high removal efficiency close to 100%, whereas at 2 g/L, the removal efficiency decreased. This result indicates that at a concentration of 1 g/L, Mn-BC removed Cd^{2+} from water more effectively. When the initial concentration was 100 or 200 mg/L, the adsorption capacity changed only slightly, suggesting that Cd^{2+} adsorption by Mn-BC stabilized. This likely occurred because the adsorption sites on the surface of Mn-BC approached saturation. Therefore, increasing the initial concentration did not significantly increase the adsorption capacity. The N_2 adsorption–desorption isotherm of Mn-BC is shown in Fig. 9b. The curve corresponded to a type-IV isotherm with an H3 hysteresis loop, likely because of the presence of mesopores and slit-shaped pores. The adsorption amount increased continuously with increasing relative pressure, indicating that the mesoporous structure provided sufficient pore space, and the hysteresis loop confirmed the presence of mesopores (Wang et al., 2024). The mesoporous structure provided Mn-BC with abundant pore channels and a high SA, thereby offering favourable conditions for Cd^{2+} adsorption. The XRD patterns of Mn-BC before and after Cd^{2+} adsorption are shown in Fig. 9c. After potassium permanganate modification, clear Mn_3O_4 peaks (PDF#: 24-0734) were identified, indicating that Mn was successfully loaded onto the surface of Mn-BC. Cd occurred in

the material mainly in a precipitated form as $CdCO_3$ (PDF#: 42–1342). The formation of $CdCO_3$ likely resulted from carbonate functional groups remaining after biochar carbonization or from dissolved CO_2 in the solution reacting with Cd^{2+} to form precipitates (Y. Zhang et al., 2023).

Before adsorption, the C 1s spectrum of Mn-BC was deconvoluted into three components, namely, 284.4 eV (C–C/C–H), 285.53 eV (C–C/C–OH), and 288.15 eV (C–O/C=O) (C 1s XPS spectra are shown in Fig. 9d). After adsorption, the relative proportion of C–C/C–H decreased from 62.89% to 49.02%, which was likely caused by Cd^{2+} adsorption.

The O 1s XPS spectra in Fig. 9e reveal that before adsorption, the O 1s peaks of Mn-BC were assigned to 532.53 eV (H_2O), 530.73 eV (M–OH), and 529.62 eV (M–O). After adsorption, the binding energy of the M–O proportion increased from 38.97% to 40.97%. The proportion of M–OH increased from 9.75% to 14.98% (a binding energy shift of ~0.15 eV), whereas the proportion of H_2O decreased from 51.28% to 44.05% (a shift of 0.11 eV). These changes could be attributed mainly to coordinated exchange between surface functional groups and Cd^{2+}, which resulted in the immobilization of Cd^{2+}. After Cd^{2+} adsorption, Mn–O–R (R: functional group) or Cd–O species formed on the surface of Mn-BC (Yin et al., 2020). The Mn $2p_{3/2}$ peak was deconvoluted into Mn(III) (641.61 eV) and Mn(IV) (642.63 eV), together with a satellite peak, indicating that Mn-BC was successfully loaded with Mn(III) and Mn(IV) (Lin et al., 2025). In the Cd XPS spectrum, the characteristic peaks of Cd $3d_{3/2}$ and Cd $3d_{5/2}$ were located at 411.57 and 404.82 eV, respectively, corresponding to CdO and

$CdCO_3$, respectively (Henríquez et al., 2023). As shown in Fig. 9g, the valence state of Cd(II) remained unchanged after adsorption, indicating that Mn-BC removed Cd(II) mainly through adsorption rather than oxidation or reduction processes (Yin et al., 2023). The Mn-BC adsorption mechanism is shown in Fig. 9h.

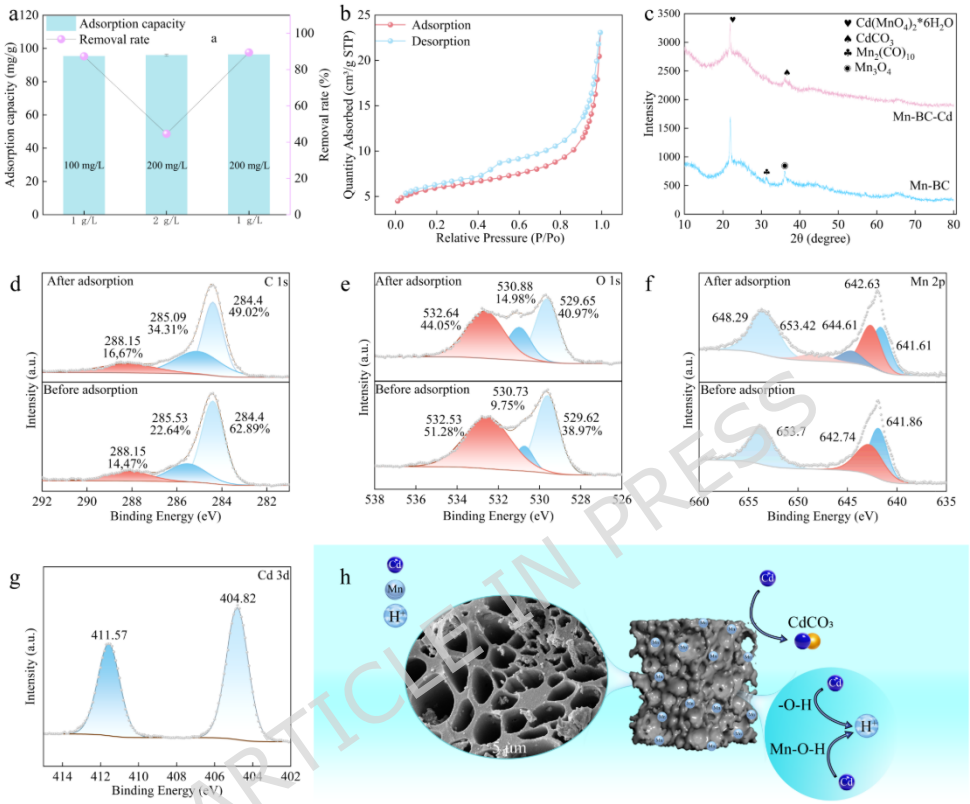

Fig 9. The adsorption capacity and removal rate of Mn-BC (a); The N_2 adsorption-desorption isotherms of Mn-BC (b); XRD (c); High-resolution XPS spectra of C 1s (d), O 1s (e), Mn 2p (f), Cd 3d (g); Adsorption mechanism diagram (h).

3.10 Prospects and limitations

In this study, ML models were employed to preliminarily explore how the preparation conditions and adsorption environment affect the Cd adsorption performance of Mn-BC, but further research remains needed. The main limitations are as follows: first, the dataset size remains relatively small. Thus, the dataset should be

expanded to enhance model stability and generalizability. Second, the current data do not cover additional microscopic material characteristics (such as functional groups and Mn content forms), which prevents a more in-depth investigation of the adsorption mechanism and creates a barrier to mechanism elucidation. This study did not focus on in-depth mechanistic analysis. In future work, advanced theoretical methods such as molecular dynamics and DFT simulations should be combined with ML methods to analyse the adsorption process at the molecular and atomic levels, thereby providing more detailed theoretical support for clarifying the mechanism underlying Cd adsorption on Mn-BC.

4. Conclusions

In this study, an ML framework for predicting the adsorption behaviour of cadmium by Mn-BC was developed. The ETR model achieved the best overall prediction performance and was subsequently employed for further interpretation and experimental verification. The model interpretation results revealed that an effective manganese–biochar design should comprehensively balance the manganese loading, pyrolysis conditions, and the retention of surface functional groups rather than merely increasing the metal content or SA. The experimental verification results in turn confirmed the applicability of the model-guided strategy. The increase in the cadmium adsorption capacity of Mn-BC was attributed mainly to the synergistic effects of surface complexation, coordination exchange, and surface precipitation. In summary, this study demonstrated that interpretable ML can be used to not only predict the adsorption performance but also provide practical guidance for the design of metal-modified

biochar adsorbents.

Supporting Information

The Supporting Information has been supplemented with the one-way partial dependence plots of each input feature in the ETR model, the Mn-BC data obtained under different conditions for model validation, the porosimetry parameters of Mn-BC, and the DOI and journal information of the cited literature. The original data have been uploaded to GitHub and are available at: https://github.com/wwwliuliuliuwww-svg/Mn-biochar-Cd-adsorption-ML.

Declaration of Competing Interest

The authors declare that they have no known competing financial interests or personal relationships that could have appeared to influence the work reported in this paper.

Acknowledgment

This work was supported by National Key Research and Development Program of China (2024YFD1600204), National Natural Science Foundation of China (42407035)□ Central Public-interest Scientific Institution Basal Research Fund.The authors extend their gratitude to Theoretical and Computational Chemistry Team from Shiyanjia Lab (www.shiyanjia.com) for providing invaluable assistance.

References

Chellappa, R., Theodoridis, S., Van Schaik, A., 2021. Advances in machine learning and deep neural networks. Proceedings of the IEEE 109, 607–611.

Chen, H., Zhang, R., Qu, X., Shan, T., Wang, Y., Zhou, R., Zhao, S., 2025. Optimizing Cu2+ adsorption prediction in Undaria pinnatifida using machine learning and isotherm models. Journal of Hazardous Materials 492, 138202.

Chen, L., Guo, L., Liao, P., Xiong, Q., Deng, X., Gao, H., Wei, H., Dai, Q., Pan, X., Zeng, Y., 2022. Effects of biochar on the dynamic immobilization of Cd and Cu and rice accumulation in soils with different acidity levels. Journal of Cleaner Production 372, 133730.

Dai, W., Xu, M., Zhao, Z., Zheng, J., Huang, F., Wang, H., Liu, C., Xiao, R., 2021a. Characteristics and quantification of mechanisms of Cd2+ adsorption by biochars derived from three different plant-based biomass. Arab. J. Chem. https://doi.org/10.1016/j.arabjc.2021.103119

Dai, W., Xu, M., Zhao, Z., Zheng, J., Huang, F., Wang, H., Liu, C., Xiao, R., 2021b. Characteristics and quantification of mechanisms of Cd2+ adsorption by biochars derived from three different plant-based biomass. Arab. J. Chem. https://doi.org/10.1016/j.arabjc.2021.103119

Dai, W., Xu, M., Zhao, Z., Zheng, J., Huang, F., Wang, H., Liu, C., Xiao, R., 2021c. Characteristics and quantification of mechanisms of Cd2+ adsorption by biochars derived from three different plant-based biomass. Arab. J. Chem. https://doi.org/10.1016/j.arabjc.2021.103119

Fan, Z., Zhang, Q., Li, M., Sang, W., Qiu, Y., Wei, X., Hao, H., 2020. Removal behavior and mechanisms of Cd (II) by a novel MnS loaded functional biochar: Influence of oxygenation. Journal of Cleaner Production 256, 120672.

Henríquez, R., Mestra-Acosta, A.S., Grez, P., Muñoz, E., Sessarego, G., Navarrete-Astorga, E., Dalchiele, E.A., 2023. High-performance asymmetric supercapacitor based on a CdCO3/CdO/Co3O4 composite supported on Ni foam – part II: a three-electrode electrochemical study. RSC Adv. https://doi.org/10.1039/d3ra00499f

Huang, H., Wei, X., Zhou, Y., 2022. An overview on twin support vector regression. Neurocomputing 490, 80–92.

Huang, J., Ashraf, W.M., Ansar, T., Abbas, M.M., Tlija, M., Tang, Y., Guo, Y., Zhang, W., 2025. Optimisation led energy-efficient arsenite and arsenate adsorption on various materials with machine learning. Water Research 271, 122815.

Jiang, X., Liu, Z., Yan, B., Zhao, L., Chen, T., Yang, X., 2024. Effects of active silicon amendment on Pb(II)/Cd(II) adsorption: Performance evaluation and mechanism. Journal of Hazardous Materials 478, 135614. https://doi.org/10.1016/j.jhazmat.2024.135614

Kong, H., Li, Q., Zheng, X., Chen, P., Zhang, G., Huang, Z., 2023a. Lanthanum modified chitosan-attapulgite composite for phosphate removal from water: Performance, mechanisms and applicability. International Journal of Biological Macromolecules 224, 984–997.

Kong, H., Wang, J., Zhang, G., Shen, F., Li, Q., Huang, Z., 2023b. Synthesis of three-dimensional porous lanthanum modified attapulgite chitosan hydrogel bead for phosphate removal: Performance, mechanism, cost-benefit analysis. Separation and Purification Technology 320, 124098.

Kong, H., Wang, W., Wang, J., Zhang, G., Shen, F., Jiang, H., Li, Q., Huang, Z., 2024. New insights into Lanthanum-Calcium bimetal for phosphate removal: Performance, molecular dynamics and life cycle assessment. Separation and Purification Technology 351, 128038.

Li, H., Shi, Y., Liu, J., Ba, Z., Liu, S., Yan, B., Liang, D., Xie, Y., 2026. Elucidating microplastic

adsorption mechanisms in biomass composite materials through interpretable machine learning. Journal of Hazardous Materials 501, 140700. https://doi.org/10.1016/j.jhazmat.2025.140700

Li, Jie, Pan, L., Huang, Y., Liu, X., Ye, Z., Wang, Y., 2024. Biochar design for antibiotics adsorption via a hybrid machine-learning-based optimization framework. Separation and Purification Technology 348, 127666.

Li, Jishuo, Xu, K., Yao, X., Liu, J., 2024. Investigation of biomass slow pyrolysis mechanisms based on the generation trends in pyrolysis products. Process Safety and Environmental Protection 183, 327–338.

Li, W., Zhang, L., Su, T., Luo, X., Xie, X., Qin, Z., 2025. Carboxymethyl cellulose sodium/bentonite composite adsorbent for Cd(II) adsorption from wastewater. Adv. Compos. Hybrid Mater. https://doi.org/10.1007/s42114-024-01185-x

Lian, W., Yang, L., Joseph, S., Shi, W., Bian, R., Zheng, J., Li, L., Shan, S., Pan, G., 2020. Utilization of biochar produced from invasive plant species to efficiently adsorb Cd (II) and Pb (II). Bioresource Technology 317, 124011. https://doi.org/10.1016/j.biortech.2020.124011

Lin, H., Li, Xiaoyin, He, J., Li, Xinru, Meng, K., Dong, Y., 2025. Fe/Mn-modified rapeseed straw biochar for selective removal of Pb2+ and Cd2+ from acid mine drainage: adsorption performance and mechanism. Journal of Analytical and Applied Pyrolysis 107393.

Liu, B., Chen, T., Wang, B., Zhou, S., Zhang, Z., Li, Y., Pan, X., Wang, N., 2022. Enhanced removal of Cd2+ from water by AHP-pretreated biochar: Adsorption performance and mechanism. Journal of Hazardous Materials 438, 129467.

Liu, C., Balasubramanian, P., An, J., Li, F., 2025. Machine learning prediction of ammonia nitrogen adsorption on biochar with model evaluation and optimization. Npj Clean Water 8, 13.

Liu, Z., He, M., Tang, L., Shao, B., Liang, Q., Wu, T., Pan, Y., Zhang, X., Luo, S., He, Q., 2023. Dual redox cycles of Mn (II)/Mn (III) and Mn (III)/Mn (IV) on porous Mn/N co-doped biochar surfaces for promoting peroxymonosulfate activation and ciprofloxacin degradation. Journal of Colloid and Interface Science 634, 255–267.

Mensah, A.K., Sekyi-Annan, E., Adams, S., Okyere, H., Issaka, F., Asante, P.C., Yakubu, H.G., Tay, C.K., 2025. Potentially toxic elements in flooded-gold-mine fields: compost stabilises Cd, biochar and manure mobilize As and Pb. Journal of Hazardous Materials 139736.

Nandi, B., Patel, G., Das, S., 2025. Machine learning prediction of flow-induced scour depth around isolated pier comparing stand-alone and ensemble models. Engineering Applications of Artificial Intelligence 156, 111318.

Neubauer, A., Brandt, S., Kriegel, M., 2024. Relationship between feature importance and building characteristics for heating load predictions. Applied Energy 359, 122668.

Qu, J., Che, N., Niu, G., Liu, L., Li, C., Liu, Y., 2023. Iron/manganese binary metal oxide-biochar nano-composites with high adsorption capacities of Cd2+: Preparation and adsorption mechanisms. Journal of Water Process Engineering 51, 103332.

Sun, L., Gong, P., Sun, Y., Qin, Q., Song, K., Ye, J., Zhang, H., Zhou, B., Xue, Y., 2022. Modified chicken manure biochar enhanced the adsorption for Cd2+ in aqueous and immobilization of Cd in contaminated agricultural soil. Science of the Total Environment 851, 158252.

Sun, Y., Liu, C., Gao, Y., Zhang, T., Jia, Y., Wang, S., 2023. All-in-one strategy to prepare molded biochar with magnetism from sewage sludge for high-efficiency removal of Cd (II). Journal of Hazardous Materials 454, 131488.

Tian, H., Peng, S., Zhao, L., Chen, Y., Cui, K., 2023. Simultaneous adsorption of Cd (II) and

degradation of OTC by activated biochar with ferrate: Efficiency and mechanism. Journal of Hazardous Materials 447, 130711.

Wang, J., Wei, X., Kong, H., Zheng, X., Guo, H., 2023. Hydrothermal Ammonia Carbonization of Rice Straw for Hydrochar to Separate Cd(II) and Zn(II) Ions from Aqueous Solution. Polymers. https://doi.org/10.3390/polym15234548

Wang, J., Wei, X., Shen, Y., Kong, H., Wang, W., Smith Jr, R.L., Guo, H., 2025. Mitigation of phosphorus contamination from livestock farms with La-containing hydrochar adsorbent. Separation and Purification Technology 359, 130465.

Wang, M., Wang, X., Zhang, M., Han, W., Yuan, Z., Zhong, X., Yu, L., Ji, H., 2023. Treatment of Cd (II) and As (V) co-contamination in aqueous environment by steel slag-biochar composites and its mechanism. Journal of Hazardous Materials 447, 130784.

Wang, Q., Yao, Y., 2025. Harnessing machine learning for high-entropy alloy catalysis: a focus on adsorption energy prediction. npj Computational Materials 11, 91.

Wang, W., Kong, H., Wang, J., Zhang, G., Shen, F., Liu, F., Huang, Z., 2024. Lanthanum-calcium bimetallic-modified attapulgite-chitosan hydrogel beads for efficient phosphate removal from water: Performance evaluation, mechanistic and life cycle assessment. Carbohydrate Polymers 338, 122183.

Wang, Y., Zeng, W., Wan, X., Wang, L., Lei, M., Chen, T., 2025. Modeling the removal of Cd (II) and Pb (II) from aqueous solutions by biochar derived from arsenic hyperaccumulator Pteris vittata. Journal of Environmental Management 381, 125280.

Wang, Z., Wang, B., Liu, Q., Huo, X., Chang, T., Sun, J., Zhao, Z., Wang, G., Liu, J., 2025. Predicting heavy metals adsorption on microplastics and unraveling the adsorption mechanism with machine learning methods. Surfaces and Interfaces 72, 107101. https://doi.org/10.1016/j.surfin.2025.107101

Wu, P., Cui, P., Zhang, Y., Alves, M.E., Liu, C., Zhou, D., Wang, Y., 2022. Unraveling the molecular mechanisms of Cd sorption onto MnOx-loaded biochar produced from the Mn-hyperaccumulator Phytolacca americana. Journal of Hazardous Materials 423, 127157.

Xiao, J., Hu, R., Chen, G., Xing, B., 2020. Facile synthesis of multifunctional bone biochar composites decorated with Fe/Mn oxide micro-nanoparticles: physicochemical properties, heavy metals sorption behavior and mechanism. Journal of Hazardous Materials 399, 123067.

Xiao, X., Chen, Z., Chen, B., 2016. H/C atomic ratio as a smart linkage between pyrolytic temperatures, aromatic clusters and sorption properties of biochars derived from diverse precursory materials. Sci. Rep. https://doi.org/10.1038/srep22644

Xu, C., Zhao, W., Ma, H., Wang, H., Wang, Y., 2022. Tailored design of well-defined hierarchical nitrogen-doped carbon via salt-confined strategy for selective Cd(II) adsorption. Chemical Engineering Journal 446, 137222. https://doi.org/10.1016/j.cej.2022.137222

Yang, H., Huang, K., Zhang, K., Weng, Q., Zhang, H., Wang, F., 2021. Predicting heavy metal adsorption on soil with machine learning and mapping global distribution of soil adsorption capacities. Environmental Science & Technology 55, 14316–14328.

Yin, G., Chen, X., Sarkar, B., Bolan, N.S., Wei, T., Zhou, H., Wang, H., 2023. Co-adsorption mechanisms of Cd (II) and As (III) by an Fe-Mn binary oxide biochar in aqueous solution. Chemical Engineering Journal 466, 143199.

Yin, G., Song, X., Tao, L., Sarkar, B., Sarmah, A.K., Zhang, W., Lin, Q., Xiao, R., Liu, Q., Wang, H., 2020a. Novel Fe-Mn binary oxide-biochar as an adsorbent for removing Cd (II) from aqueous

solutions. Chemical Engineering Journal 389, 124465.
Yin, G., Song, X., Tao, L., Sarkar, B., Sarmah, A.K., Zhang, W., Lin, Q., Xiao, R., Liu, Q., Wang, H., 2020b. Novel Fe-Mn binary oxide-biochar as an adsorbent for removing Cd(II) from aqueous solutions. Chemical Engineering Journal 389, 124465. https://doi.org/10.1016/j.cej.2020.124465
Yuan, X., Suvarna, M., Low, S., Dissanayake, P.D., Lee, K.B., Li, J., Wang, X., Ok, Y.S., 2021. Applied machine learning for prediction of CO2 adsorption on biomass waste-derived porous carbons. Environmental Science & Technology 55, 11925–11936.
Zhang, H., Huang, H., Fang, Y., Cai, J., Lv, X., Wu, W., Gu, Q., Qian, R., Yu, K., Tang, K.H.D., 2025. Synthesis of magnetic biochar co-doped with sulfur, iron, and manganese via a novel modification method for simultaneous Cd and Pb remediation. Separation and Purification Technology 363, 132025.
Zhang, H., Xu, F., Xue, J., Chen, S., Wang, J., Yang, Y., 2020. Enhanced removal of heavy metal ions from aqueous solution using manganese dioxide-loaded biochar: Behavior and mechanism. Sci. Rep. https://doi.org/10.1038/s41598-020-63000-z
Zhang, J., Fu, K., Wang, D., Zhou, S., Luo, J., 2024. Refining hydrogel-based sorbent design for efficient toxic metal removal using machine learning-Bayesian optimization. Journal of Hazardous Materials 479, 135688.
Zhang, J., Ma, X., Yuan, L., Zhou, D., 2020. Comparison of adsorption behavior studies of Cd2+ by vermicompost biochar and KMnO4-modified vermicompost biochar. Journal of Environmental Management 256, 109959.
Zhang, L., Ren, Y., Xue, Y., Cui, Z., Wei, Q., Han, C., He, J., 2020. Preparation of biochar by mango peel and its adsorption characteristics of Cd(II) in solution. RSC Adv. https://doi.org/10.1039/d0ra06586b
Zhang, R., Liu, S., Lian, C., Yu, J., Lin, S., 2025. Machine Learning-Accelerated Design of High-Efficient Lithium Adsorbents for Salt Lake Brines. Angewandte Chemie 137, e202503644.
Zhang, W., Chen, R., Li, J., Huang, T., Wu, B., Ma, J., Wen, Q., Tan, J., Huang, W., 2023. Synthesis optimization and adsorption modeling of biochar for pollutant removal via machine learning. Biochar 5, 25.
Zhang, Y., Li, A., Liu, L., Duan, X., Ge, W., Liu, C., Qiu, G., 2023. Enhanced remediation of cadmium-polluted soil and water using facilely prepared MnO2-coated rice husk biomass. Chemical Engineering Journal 457, 141311.
Zhao, C., Zhang, J., Zhang, W., Yang, Y., Guo, D., Zhang, H., Liu, L., 2024a. Reveal the main factors and adsorption behavior influencing the adsorption of pollutants on natural mineral adsorbents: Based on machine learning modeling and DFT calculation. Separation and Purification Technology 331, 125706.
Zhao, C., Zhang, W., Zhang, Y., Yang, Y., Guo, D., Liu, W., Liu, L., 2024b. Influence of multivalent background ions competition adsorption on the adsorption behavior of azo dye molecules and removal mechanism: Based on machine learning, DFT and experiments. Separation and Purification Technology 341, 126810.
Zhao, Shuyan, Guo, J., Tang, Y., Zhou, Y., 2025. Applications of machine learning in heavy metal adsorption modeling: A review. Separation and Purification Technology 134168.
Zhao, Shilin, Liu, Q., Wang, Y., Wang, L., Zhang, J., Sun, Z., 2025. Machine Learning-Assisted Prediction of Mercury Removal Efficiency of Carbon-Based Adsorbents. Environmental Science & Technology 59, 17677–17687.